Correlating structural distributions in silica glass with two-dimensional *J*-resolved spectroscopy

Deepansh J. Srivastava
Department of Chemistry, Ohio State University, 100 West 18th Avenue, Columbus, Ohio 43210, USA

Jay H. Baltisberger
Division of Natural Science, Mathematics, and Nursing, Berea College, Berea, Kentucky 40403, USA

Pierre Florian, Franck Fayon, Roman A. Shakhovoy, and Michaël Deschamps
CNRS, UPR3079 CEMHTI, 1D Avenue de la Recherche Scientifique, 45071 Orléans Cedex 2, France

Najim Sadiki
PROMES, CNRS, Rambla de la Thermodynamique, Tecnosud, 66100 Perpignan, France

Philip J. Grandinetti*
Department of Chemistry, Ohio State University, 100 West 18th Avenue, Columbus, Ohio 43210, USA

(Received 15 March 2018; revised manuscript received 16 July 2018; published 8 October 2018)

A two-dimensional (2D) *J*-resolved magic-angle spinning nuclear magnetic resonance (NMR) spectrum of silica glass at ^{29}Si natural abundance levels, 4.7%, was measured using the shifted-echo phase-incremented echo train acquisition (SE-PIETA) pulse sequence. At ^{29}Si natural abundance levels the $J_{\text{Si-O-Si}}$ coupling splittings appear as overlapping doublet patterns arising from isolated ^{29}Si-O-^{29}Si linkages. The experimental 2D *J*-resolved spectrum is analyzed to obtain a bivariate probability distribution correlating the central Si-O-Si angle of a Q^4-Q^4 linkage to its mean Si-O-Si angle (seven angles) using relationships between ^{29}Si isotropic chemical shifts and geminal $J_{\text{Si-O-Si}}$ coupling of a Q^4-Q^4 to its local structure. To obtain a self-consistent bivariate probability distribution it was necessary to introduce an additional dependence of the ^{29}Si chemical shift of a Q^4 on mean Si-O distance as well as mean Si-O-Si angle. The implication of this necessary modification is a positive correlation between Si-O-Si angle and Si-O distance in the silica glass, consistent with recent ^{17}O NMR measurements on ambient and densified silica glasses but running opposite to the trend generally found in crystalline silica polymorphs. From the analysis of the ^{29}Si 2D *J*-resolved spectrum we determine a Si-O-Si bond angle distribution in silica glass as having a mean at 147.8°, a mode at 147°, and a standard deviation of 10.7°. Our statistical model for analyzing the experimental ^{29}Si 2D *J*-resolved spectrum also indicates that the individual Si-O-Si bond angle distributions are relatively uncorrelated.

DOI: 10.1103/PhysRevB.98.134202

I. INTRODUCTION

Glass structure is a difficult thing to characterize. Any structural model of glass is necessarily statistical in nature; that is, the individual atomic positions cannot be known. When constructing structural models of glasses the most commonly used prior information comes from the static structure factors obtained from diffraction measurements [1,2], whose Fourier transform is the pair (2-body) correlation function of the material. Unfortunately, in the case of a glass this one-dimensional statistical distribution is smooth and provides few structural constraints [3]. While techniques like reverse Monte Carlo [4] and recent variants [5,6] rely solely on experimental information, the unfortunate truth is that the information content of most experimental measurements on glass structure is low. Recently devised hybrid methods attempt to incorporate additional prior information from classical and *ab initio* potentials. The challenge with this approach, however, is in finding accurate potentials that are transferable to structural studies of glasses when they are trained on crystalline databases [3,7].

Here we focus on the experimental side of the problem by attempting to increase the information content of measurements through the use of more sophisticated multidimensional nuclear magnetic resonance (NMR) spectroscopy measurements and spectral analysis. We illustrate this approach in the case of the archetypical network-forming glass, vitreous SiO_2. In the majority of NMR studies of network-forming glasses, where spectra contain a number of resolved "resonances," spectroscopists focus almost entirely on using NMR spectra to identify and quantify populations of polyhedral units, and polyhedral linkages [8]. This coarse-grain analysis has generated tremendous insight into the structure of glass over the last 30 years, yet it falls short in exploring the full range of noteworthy structural distributions. By using the term "coarse-grain analysis" and referring to "resonances" in quotes, we are highlighting the fact that these resolved "resonances" are inhomogeneously broadened; that is, inside

*Corresponding author: www.grandinetti.org

each "resonance" is a mix of homogeneous resonances from numerous structurally distinct sites. The shape of these inhomogeneous "resonances" contains a wealth of structural information, and it is two mappings: (1) from NMR line shape to probability distribution of NMR parameters, and (2) from NMR parameter distribution to probability distribution of structure parameters that lie at the heart of more refined structural assignments of glass NMR spectra. We refer to such a quantitative spectral analysis that produces a probability distribution for glass structure parameters as a "fine-grain" analysis.

One of the first attempts to perform a fine-grain analysis of an inhomogeneous NMR line shape from a glass was in 1984 by Dupree and Pettifer [9] on the ^{29}Si magic-angle spinning (MAS) spectrum of silica glass. Using then-recently established correlations between ^{29}Si isotropic chemical shift and the mean Si-O-Si angle of a tetrahedron, Dupree and Pettifer inverted the MAS line shape of a Q^4 resonance into the Si-O-Si angle distribution of silica. While a direct inversion of the ^{29}Si MAS spectrum of silica glass yields the distribution of mean Si-O-Si angles of the Q^4 sites, the individual Si-O-Si bond angle distribution can be obtained in a more sophisticated analysis with the assumption that the four Si-O-Si angles on each Q^4 are statistically independent [9–11]. Unfortunately, in more compositionally diverse silicate glasses the correlation between ^{29}Si isotropic chemical shift and the mean Si-O-Si angle becomes strongly influenced by the identity of the next-nearest-neighbor polyhedral units and modifier cations, and the line shape inversion is no longer as simple. These caveats aside, the Dupree and Pettifer study pointed the way towards more systematic inversions of glass spectra.

While NMR spectroscopy of glasses generally suffers the same malady of overlapping resonances as other spectroscopies, NMR has a distinct advantage of not being limited to one spectroscopic dimension. In 1992 Farnan *et al.* [12] used dynamic-angle spinning [13–16] (DAS) NMR to measure the isotropic ^{17}O NMR line shape of the bridging oxygen in a potassium tetrasilicate glass. Although there is no simple mapping between the ^{17}O isotropic shift and Si-O-Si angle, they showed that the correlated anisotropic line shapes from the full two-dimensional (2D) DAS spectrum can be used to extract mean quadrupolar coupling parameters for each correlated part of the inhomogeneous isotropic line shape. The quadrupolar asymmetry parameter, for which correlations to Si-O-Si angle were known, was then used to invert the isotropic line shape into the mean Si-O-Si angle distribution of the potassium tetrasilicate glass.

Since the work of Farnan *et al.* [12] considerable progress has been made in determining more precise relationships between the ^{17}O nuclear quadrupolar coupling parameters of the intertetrahedral bridging oxygen and its first coordination sphere structure [17–27]. A particular advantage of ^{17}O 2D DAS is that it can now determine the bivariate distribution of Si-O distances and Si-O-Si angles. In the case of silica this advance was significant because it revealed a strong positive correlation, i.e., Si-O distance increasing with increasing Si-O-Si angle [28,29]. This correlation runs counter to conventional wisdom of a negative correlation in silicate glass structure. Further evidence of this positive correlation could impact our understanding of the role of configuration entropy in stabilizing certain silicate glass structures [30].

In this work we develop an approach for determining the bivariate probability distribution correlating the central Si-O-Si angle of a Q^4-Q^4 linkage to its mean Si-O-Si angle (seven angles) using relationships between ^{29}Si isotropic chemical shifts and geminal $J_{\text{Si-O-Si}}$ coupling of a Q^4-Q^4 to its local structure. While J couplings are a powerful probe of structure in liquid-state NMR spectroscopy, they have seen limited use in solid-state NMR studies. This is because (1) the J splittings are often tiny compared to linewidths in solid-state magic-angle spinning (MAS) NMR and, therefore, difficult to detect, and (2) our understanding of the relationships between J couplings and local structure had lagged behind other NMR probes of structure, such as chemical shifts and nuclear quadrupole couplings. An important advance in solving the first problem occurred in 2012 with the development of a new NMR method called phase-incremented echo train acquisition (PIETA), which not only removes the inhomogeneous broadenings obscuring J splittings in MAS spectra but also is a method for rapid and sensitive measurement of a 2D J-resolved spectrum [31]. More recently, Srivastava *et al.* [32] have addressed the second problem in discovering a robust relationship for converting a geminal $^2J_{\text{Si-O-Si}}$ coupling into an intertetrahedral Si-O-Si angle.

In a previous attempt by Florian *et al.* [33] in 2009, J-resolved spectra of ^{29}Si-enriched crystalline and glassy $CaSiO_3$ were measured. Due to ^{29}Si enrichment, the spectrum resulted in J multiplets (Q^2) for crystalline wollastonite whereas the J multiplets rendered the J-resolved spectrum featureless in $CaSiO_3$ glass. The number of resonances in a J multiplet increase as 2^n with n neighboring ^{29}Si. Thus, the degree of complexity introduced to the spectrum by the J multiplets increases with $Q^1 < Q^2 < Q^3 < Q^4$. Since silica glass is entirely Q^4, 100% ^{29}Si enrichment gives the worst-case scenario. To make the spectra analysis more tractable we take on the experimental challenge of measuring the 2D J-resolved spectrum in silica glass at ^{29}Si natural abundance levels, 4.7%, where, instead of the overlapping multiplet patterns [33] in ^{29}Si-enriched samples, the J splittings appear as simpler overlapping doublet patterns arising from isolated ^{29}Si-O-^{29}Si linkages. Another advantage of natural abundance is that the homonuclear dipolar coupling between ^{29}Si is easily removed with MAS due to its inhomogeneous nature [34]. Most importantly, we develop and present a detailed spectral analysis for mapping the 2D J-resolved spectrum into the bivariate probability distribution correlating the central Si-O-Si angle of a Q^4-Q^4 linkage to its mean Si-O-Si angle (seven angles) in silica glass which is significantly more information rich than the one-dimensional Si-O-Si angle distribution.

II. THEORETICAL BACKGROUND

A. *J* coupling under echo train acquisition

A theoretical treatment of the detection of homonuclear J coupling between spin 1/2 nuclei using echo train acquisition in the context of liquid state NMR [35,36] has been given by Allerhand [35]. For two spin 1/2 nuclei coupled through the

J interaction, the modulation of the nth echo predominantly follows

$$s(n) \propto \cos\left[\pi J n 2\tau - n \sin^{-1}\left\{\frac{J \sin(\pi R\, 2\tau)}{R}\right\}\right], \quad (1)$$

where

$$R = (\Delta\nu^2 + J^2)^{1/2}. \quad (2)$$

Here 2τ is the interecho period and $\Delta\nu$ is the difference in the chemical shifts of the J-coupled spins. From Eq. (1) one finds the well known behavior that the echo modulation frequency disappears as the strong-coupling limit, where $J \gg \Delta\nu$, is approached,

$$\lim_{R\to J} s(n) \to 1. \quad (3)$$

All resonances close to the strong-coupling limit exhibit modulation frequencies of or near 0 Hz.

From Eq. (1) one can also find in the weak-coupling limit, where $J \ll \Delta\nu$, that

$$s(n) \propto \cos\{\pi J n 2\tau[1 - \mathrm{sinc}(\pi R\, 2\tau)]\}. \quad (4)$$

It is critical to be aware of two limiting behaviors for echo train acquisition in the weak-coupling limit. When 2τ is large, or more specifically, $\mathrm{sinc}(\pi R\, 2\tau) \ll 1$, this expression simplifies to the expected behavior,

$$\lim_{2\tau\to\infty} s(n) \to \cos(\pi J n 2\tau). \quad (5)$$

On the other hand, in the limit that 2τ goes to zero, i.e., $\mathrm{sinc}(\pi R\, 2\tau) = 1$, the echo modulation frequency disappears,

$$\lim_{2\tau\to 0} s(n) \to 1. \quad (6)$$

Thus, even in the weak-coupling limit, the J modulation during echo train acquisition deviates from the expected behavior of Eq. (5), instead giving, according to Eq. (4), a τ-dependent echo modulation frequency (sinc function variation of the J splitting) when the interecho period is short relative to the inverse of the shift difference. The influence of this effect diminishes as $1/(\pi\Delta\nu\, 2\tau)$. In this study the majority of the ^{29}Si-^{29}Si pairs fall in the weak-coupling limit and we show that only a small fraction (see below) are lost due to being in the strong-coupling limit or having frequency shift differences that are small compared to $1/(2\tau)$.

B. Pulse sequence

The shifted-echo phase-incremented echo train acquisition (SE-PIETA) pulse sequence is shown in Fig. 1. We describe this sequence using the symmetry pathway formalism [37] which generalizes the concept of coherence transfer pathways [38] to the "spatial pathway," which maps into a set of *spatial symmetry pathways*, and the "transition pathway," which maps into a set of *transition symmetry pathways*. In the case of weak J coupling between dilute ^{29}Si-^{29}Si pairs under fast magic-angle spinning (MAS) the rotating frame transition frequency is given by

$$\Omega_{AX} = -\omega_0\sigma_{\mathrm{iso},A}\,\mathbb{p}_A - \omega_0\sigma_{\mathrm{iso},X}\,\mathbb{p}_X - 2\pi J_{AX}\,\mathbb{d}_{AX}, \quad (7)$$

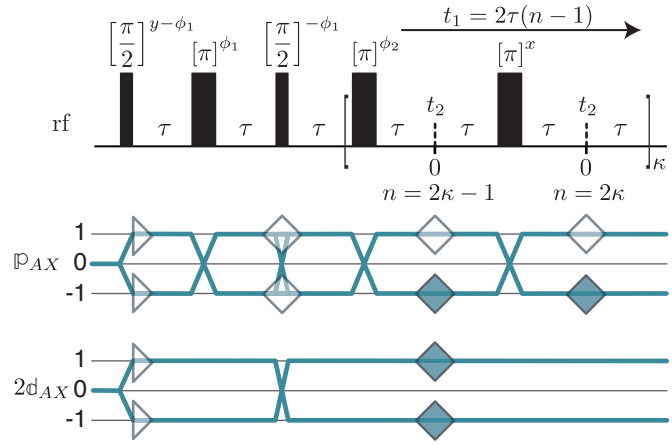

FIG. 1. Graphical representation of the shifted-echo PIETA sequence and relevant symmetry pathways. Here $\kappa = 1, \ldots, N$ and $n = 1, \ldots, 2N$ is the echo counter where $2N$ is the number of echoes acquired.

where the transition symmetry functions are given by

$$\begin{aligned}\mathbb{p}_A &= m_{A,j} - m_{A,i},\\ \mathbb{p}_X &= m_{X,j} - m_{X,i},\\ \mathbb{d}_{AX} &= m_{A,j}m_{X,j} - m_{A,i}m_{X,i}.\end{aligned} \quad (8)$$

Here $\sigma_{\mathrm{iso},A}$ and $\sigma_{\mathrm{iso},X}$ are the isotropic nuclear shieldings, ω_0 is the Larmor frequency, and J_{AX} is the indirect-coupling constant. The quantum numbers, m_A and m_X, are associated with quantized energy levels of A and X nuclei, respectively, while i and j represent the initial and final energy state of the NMR transition. The $\mathbb{p}_A$, $\mathbb{p}_X$, and $\mathbb{d}_{AX}$ values for single quantum transitions in a system of two weakly coupled spin 1/2 nuclei are shown in Fig. S1 of the Supplemental Material [39]. In the case of two weakly coupled homonuclear nuclei it is useful to define the additional transition symmetry function $\mathbb{p}_{AX} = \mathbb{p}_A + \mathbb{p}_X$. The $\mathbb{p}_A$, $\mathbb{p}_X$, and $\mathbb{d}_{AX}$ spin transition symmetry functions reflect their symmetry under the orthogonal rotation subgroup where simple rules hold under a π pulse, such as that the $\mathbb{d}_{AX}$ spin transition symmetry function is invariant, whereas $\mathbb{p}_A$, $\mathbb{p}_X$, and $\mathbb{p}_{AX}$ spin transition symmetry functions change sign.

The SE-PIETA sequence separates and correlates the third frequency term in Eq. (7), the weak J coupling, with the isotropic ^{29}Si chemical shifts of the first and second terms in Eq. (7). This sequence is based on the PIETA method for obtaining a 2D J-resolved spectrum in a "pseudo-single-scan" experiment [31], "single scan" in the sense that the entire multidimensional time domain signal is acquired in a single acquisition, and "pseudo" because the separate "single-scan" signals must also be acquired along an rf pulse phase dimension. Sampling in the rf pulse phase dimension, however, need not increase the total experiment time since it is performed in lieu of conventional phase cycling and signal averaging.

The shifted-echo modification of the sequence eliminates a signal artifact when using the original PIETA experiment for 2D J-resolved spectroscopy which arises from an inability to acquire a full echo for the $t_1 = 0$ ($n = 1$) cross section. Using the shifted-echo approach [16,37], in the case of 2D

J-resolved spectroscopy, requires a simultaneous echo of both $\mathbb{p}$ and $\mathbb{d}$ transition symmetries at $t_1 = 0$. It is well known [40–42] that such a simultaneous echo in the case of two weakly coupling nuclei can be generated with the sequence

$$\text{equilibrate} - \frac{\pi}{2} - \tau - \pi - \tau - \frac{\pi}{2} - \tau - \pi - \tau \rightarrow \bullet. \quad (9)$$

The first $\pi/2$ pulse on a system of two weakly coupled spin 1/2 nuclei excites all eight single quantum transitions, shown in Fig. S1, which then evolves for a period τ. Next, the π pulse converts the transition $|m_{A,j}, m_{X,j}\rangle\langle m_{A,i}, m_{X,i}|$ entirely into the transition $|-m_{A,j}, -m_{X,j}\rangle\langle -m_{A,i}, -m_{X,i}|$ leaving the number of transition pathways after the π pulse at eight. By the end of the second τ period all chemical shift evolution phases on these 8 transition pathways refocus into an echo. At this point these eight transition pathways can be divided into two sets of four with the first set having the same negative J (or $\mathbb{d}_{AX}$) evolution:

$$\begin{array}{cccc} \underbrace{A_2^* \xrightarrow{\pi} A_1,} & \underbrace{X_2^* \xrightarrow{\pi} X_1,} & \underbrace{A_1 \xrightarrow{\pi} A_2^*,} & \underbrace{X_1 \xrightarrow{\pi} X_2^*} \\ \mathbb{p}_{AX} = +1 \rightarrow -1 & & \mathbb{p}_{AX} = -1 \rightarrow +1 & \\ 2\mathbb{d}_{AX} = -1 \rightarrow -1 & & 2\mathbb{d}_{AX} = -1 \rightarrow -1 & \end{array}, \quad (10)$$

and the other set having the same positive J (or $\mathbb{d}_{AX}$) evolution:

$$\begin{array}{cccc} \underbrace{A_1^* \xrightarrow{\pi} A_2,} & \underbrace{X_1^* \xrightarrow{\pi} X_2,} & \underbrace{A_2 \xrightarrow{\pi} A_1^*,} & \underbrace{X_2 \xrightarrow{\pi} X_1^*} \\ \mathbb{p}_{AX} = +1 \rightarrow -1 & & \mathbb{p}_{AX} = -1 \rightarrow +1 & \\ 2\mathbb{d}_{AX} = +1 \rightarrow +1 & & 2\mathbb{d}_{AX} = +1 \rightarrow +1 & \end{array}. \quad (11)$$

The second $\pi/2$ pulse has a similar effect to that in a solid echo experiment [43], which is to transfer coherence only between single quantum transitions with opposite signs of $\mathbb{d}_{AX}$ [44]. As the $\mathbb{d}_{AX}$ values of transitions remain invariant under the second π pulse while the $\mathbb{p}_{AX}$ symmetries refocus again into an echo there will be a simultaneous echo of both $\mathbb{p}_{AX}$ and $\mathbb{d}_{AX}$ symmetries at the end of the fourth τ period as shown in Fig. 1. With perfect $\pi/2$ and π rotations the transition pathways in two weakly coupled nuclei generate the simultaneous echo at $t_1 = 0$ with no loss of intensity to other transition pathways.

After the formation of the simultaneous echo the chemical shift evolution can be continually refocused by a train of π pulses into echoes whose modulation by J evolution leads to the desired doublet splitting. The 16 detectable pathways with $2\Delta\mathbb{d}_{AX} = +2$, leading to the nth echo, are given in condensed notation below,

$$\left.\begin{array}{l} A_2^* \xrightarrow{\pi} A_1 \xrightarrow{\frac{\pi}{2}} \\ X_2^* \xrightarrow{\pi} X_1 \xrightarrow{\frac{\pi}{2}} \\ A_1 \xrightarrow{\pi} A_2^* \xrightarrow{\frac{\pi}{2}} \\ X_1 \xrightarrow{\pi} X_2^* \xrightarrow{\frac{\pi}{2}} \end{array}\right\} \otimes \left\{\begin{array}{l} A_1^* [\xrightarrow{\pi} A_2(t_2) \xrightarrow{\pi} A_1^*]_\kappa, \\ X_1^* [\xrightarrow{\pi} X_2(t_2) \xrightarrow{\pi} X_1^*]_\kappa, \\ A_2 [\xrightarrow{\pi} A_1^* \xrightarrow{\pi} A_2(t_2)]_\kappa, \\ X_2 [\xrightarrow{\pi} X_1^* \xrightarrow{\pi} X_2(t_2)]_\kappa, \end{array}\right. \quad (12)$$

and the 16 detectable pathways with $2\Delta\mathbb{d}_{AX} = -2$, leading to the nth echo, are similarly given by

$$\left.\begin{array}{l} A_1^* \xrightarrow{\pi} A_2 \xrightarrow{\frac{\pi}{2}} \\ X_1^* \xrightarrow{\pi} X_2 \xrightarrow{\frac{\pi}{2}} \\ A_2 \xrightarrow{\pi} A_1^* \xrightarrow{\frac{\pi}{2}} \\ X_2 \xrightarrow{\pi} X_1^* \xrightarrow{\frac{\pi}{2}} \end{array}\right\} \otimes \left\{\begin{array}{l} A_2^* [\xrightarrow{\pi} A_1(t_2) \xrightarrow{\pi} A_2^*]_\kappa, \\ X_2^* [\xrightarrow{\pi} X_1(t_2) \xrightarrow{\pi} X_2^*]_\kappa, \\ A_1 [\xrightarrow{\pi} A_2^* \xrightarrow{\pi} A_1(t_2)]_\kappa, \\ X_1 [\xrightarrow{\pi} X_2^* \xrightarrow{\pi} X_1(t_2)]_\kappa, \end{array}\right. \quad (13)$$

where t_2 next to a transition represents acquisition of an echo. A full expansion of these 32 transition pathways is given in the Supplemental Material [39].

The symmetry pathways associated with these transition pathways are

$$\begin{aligned} \mathbb{p}_{AX} &= 0 \xrightarrow{\frac{\pi}{2}} +1 \xrightarrow{\pi} -1 \xrightarrow{\frac{\pi}{2}} +1 [\xrightarrow{\pi} -1(t_2) \xrightarrow{\pi} +1]_\kappa, \\ 2\mathbb{d}_{AX} &= 0 \xrightarrow{\frac{\pi}{2}} \mp 1 \xrightarrow{\pi} \mp 1 \xrightarrow{\frac{\pi}{2}} \pm 1 [\xrightarrow{\pi} \pm 1(t_2) \xrightarrow{\pi} \pm 1]_\kappa, \end{aligned} \quad (14)$$

$$\begin{aligned} \mathbb{p}_{AX} &= 0 \xrightarrow{\frac{\pi}{2}} +1 \xrightarrow{\pi} -1 \xrightarrow{\frac{\pi}{2}} -1 [\xrightarrow{\pi} +1 \xrightarrow{\pi} -1(t_2)]_\kappa, \\ 2\mathbb{d}_{AX} &= 0 \xrightarrow{\frac{\pi}{2}} \mp 1 \xrightarrow{\pi} \mp 1 \xrightarrow{\frac{\pi}{2}} \pm 1 [\xrightarrow{\pi} \pm 1 \xrightarrow{\pi} \pm 1(t_2)]_\kappa, \end{aligned} \quad (15)$$

$$\begin{aligned} \mathbb{p}_{AX} &= 0 \xrightarrow{\frac{\pi}{2}} -1 \xrightarrow{\pi} +1 \xrightarrow{\frac{\pi}{2}} +1 [\xrightarrow{\pi} -1(t_2) \xrightarrow{\pi} +1]_\kappa, \\ 2\mathbb{d}_{AX} &= 0 \xrightarrow{\frac{\pi}{2}} \mp 1 \xrightarrow{\pi} \mp 1 \xrightarrow{\frac{\pi}{2}} \pm 1 [\xrightarrow{\pi} \pm 1(t_2) \xrightarrow{\pi} \pm 1]_\kappa, \end{aligned} \quad (16)$$

$$\begin{aligned} \mathbb{p}_{AX} &= 0 \xrightarrow{\frac{\pi}{2}} -1 \xrightarrow{\pi} +1 \xrightarrow{\frac{\pi}{2}} -1 [\xrightarrow{\pi} +1 \xrightarrow{\pi} -1(t_2)]_\kappa, \\ 2\mathbb{d}_{AX} &= 0 \xrightarrow{\frac{\pi}{2}} \mp 1 \xrightarrow{\pi} \mp 1 \xrightarrow{\frac{\pi}{2}} \pm 1 [\xrightarrow{\pi} \pm 1 \xrightarrow{\pi} \pm 1(t_2)]_\kappa. \end{aligned} \quad (17)$$

Because the second $\pi/2$ must allow both $\Delta\mathbb{p}_{AX} = 0$ and $\Delta\mathbb{p}_{AX} = \pm 2$ it is necessary to implement separate phase dimensions for the preparation sequence of Eq. (9) and the echo train acquisition as shown in Fig. 1. A Fourier transform of the signal, $s(\phi_1, \phi_2, n, t_2)$, with respect to the pulse phases ϕ_1 and ϕ_2 transforms the signal to $s'(\Delta p_1, \Delta p_2, n, t_2)$ where the two desired pathway signals at nth echo appear at the coordinates

$$\begin{array}{ll} \{\Delta p_1, \Delta p_2\}_n = & \{3(-1)^{n-1},\ 2(-1)^n \lceil n/2 \rceil\}, \\ \{\Delta p_1, \Delta p_2\}_n = & \{5(-1)^n,\ \ 2(-1)^n \lceil n/2 \rceil\}. \end{array} \quad (18)$$

Here Δp_1 is the accumulated change in coherence order through the first three pulses while Δp_2 is the accumulated change in coherence order through the subsequent π pulses leading up to the nth echo and $\lceil \cdots \rceil$ is the ceiling function. Because desired signal along the Δp_1 dimension is always sampled at either ± 3 or ± 5 for all n, we show in the Supplemental Material [39] an improved pulse sequence where the ϕ_1 phase dimension is replaced by a phase cycling scheme.

III. METHODS AND ANALYSIS

A. Sample preparation

The glass was synthesized starting from SiO_2 (99.7%; Strem Chemicals) and cobalt (II) carbonate hydrate ($CoCO_3 \cdot xH_2O$) (99.99%; Aldrich). The latter was first heat-treated in an alumina crucible for one hour at 800 °C to eliminate anionic impurities (and H_2O). The same heat treatment was applied after the mixing and before melting. The mixed starting components were melted for approximately 2 min on a water-cooled aluminum plate connected to a vertical laboratory solar furnace of 2 kW power and heat flux of 900–1000 W/m^2. Within a few seconds the temperature reached around 1900 °C (±50 °C) and instantaneous melting was observed without the formation of bubbles or any visible precipitates. Some fumes were observed, indicating vaporization of SiO_2, which are expected in an oxidizing atmosphere [45]. Transparent quasispherical blue glassy droplets between 2–5 mm in diameter were obtained after melting. The glass composition was determined by SEM-EDX analysis (Hitachi S 4500, EDS: Kevex) after a metallization with gold using the beam energy of 20 keV. With no cobalt signal detected, its amount is estimated to be less than a few 100 ppm.

B. NMR spectroscopy

The experiment was performed on a Bruker Avance III HD 400 MHz NMR spectrometer operating at 9.4 T, with a ^{29}Si Larmor frequency of 79.40716 MHz, using a 4 mm rotor spinning at 14.286 kHz. The chemical shift was referenced with respect to TMS at 0 ppm. The radio-frequency field strength was set to 53.7 kHz with a t_{90° of 4.65 μs. The magic angle was set accurately to within 0.002° using STMAS [46,47] on $RbNO_3$. This procedure provides better accuracy than the KBr spinning sidebands based procedure and removes residual ^{29}Si-^{29}Si dipolar couplings in the ^{29}Si 2D J-resolved experiments.

The four-dimensional pulse sequence shown in Fig. 1 was implemented, with a time dimension, t_2, an echo count dimension, n, and two phase dimensions, ϕ_1 and ϕ_2. The pulse phase increment was set to $\pi/6$ and $\pi/128$ for the phase dimensions, ϕ_1 and ϕ_2, with 12 and 256 phase points, respectively. A total of 254 echoes were collected with a recovery period of 60 s. The dwell time was set at 40 μs. The interecho period, 2τ, was set to 40 ms. A total of 16 scans were averaged for a total experiment time of 40 days. The Bruker pulse sequence for the shifted-echo PIETA sequence is available in the Supplemental Material [39].

C. Signal processing

All signal processing was performed with RMN [48]. A two-dimensional Fourier transform was performed on the four-dimensional signal, $s(\phi_1, \phi_2, n, t_2)$, with respect to the two phase dimensions, ϕ_1 and ϕ_2, transforming to $s'(\Delta p_1, \Delta p_2, n, t_2)$. The signal corresponding to the desired $\{\Delta p_1, \Delta p_2\}_n$ coordinates in Eq. (18) were retained in $s'(\Delta p_1, \Delta p_2, n, t_2)$ whereas signals at all other $\{\Delta p_1, \Delta p_2\}_n$ coordinates were zeroed. Next, a projection onto the Δp_1 dimension followed by a projection onto the Δp_2 dimension was performed. From the resulting two-dimensional echo count n vs time t_2 signal, $s''(n, t_2)$, the echo count dimension n was converted to the echo time dimension, t_1, using the relationship

$$t_1 = 2\tau(n-1). \tag{19}$$

The formation of simultaneous $\mathbb{p}_{AX}$ and $\mathbb{d}_{AX}$ echo occurs at $t_1 = t_2 = 0$. A step-by-step graphical illustration of this processing is given in the Supplemental Material [39]. Alternatively, a MATLAB script that performs a postacquisition "phase cycling" down to a conventional 2D J-resolved signal, $s''(t_1, t_2)$, is also made available in the Supplemental Material [39].

A two-dimensional Fourier transform was performed on $s''(t_1, t_2)$, transforming the time dimension, t_2, into the ^{29}Si MAS dimension and echo time dimension, t_1, into the J-resolved dimension. Next, a shear of -45° was performed along the ^{29}Si MAS dimension to transform it into a pure ^{29}Si isotropic chemical shift dimension, δ. The resulting ^{29}Si 2D J-resolved spectrum is shown in Fig. 2(a).

D. ^{29}Si isotopomer statistics

Of the three stable isotopes of silicon, ^{28}Si is the most abundant at 92.23%, followed by ^{29}Si at 4.67%, and ^{30}Si at 3.1%. Of these only ^{29}Si is NMR active with $I = 1/2$. To predict the relative intensity of all possible J multiplets in the ^{29}Si NMR spectrum of silica glass we start with the probability that n of the four Si atoms connected to a $^{29}SiO_4$ tetrahedron in silica glass are ^{29}Si nuclei,

$$P_n = \binom{4}{n} p^n (1-p)^{(4-n)}, \tag{20}$$

where $p = 0.0467$ is the natural abundance of ^{29}Si. This expression predicts that the relative intensity of J multiplets decrease rapidly with increasing n, with $P_0 = 0.826$ for the uncoupled resonance, $P_1 = 0.162$ for the two-spin multiplet, $P_2 = 0.0119$ for the three-spin multiplet, $P_3 = 0.000388$ for the four-spin multiplet, and $P_4 = 4.76 \times 10^{-6}$ for the five-spin multiplet. While the ^{29}Si NMR spectrum of silica glass contains contributions from all five cases we can confidently take the observed intensity as arising entirely from the uncoupled and two-spin doublet resonances. Thus while the sum of the P_n is 1 we can approximately terminate the sum at P_1:

$$\sum_n P_n \approx P_0 + P_1 \approx 1. \tag{21}$$

In Eq. (7) and Sec. II, we considered the resonances from an ideal case of two weakly J-coupled spin 1/2 nuclei where the only interactions were isotropic chemical shifts of the two nuclei and the J coupling between them. In the solid state, however, the chemical shift anisotropies (CSAs) and dipolar couplings also play an important role in the detection of J couplings. In a simple Hahn echo experiment a two-coupled spin system in the solid state behaves identical to that of solution-state NMR [49] in the fast-MAS limit [50] where

$$|\nu_r| > |d\Delta\nu/2\pi J|, |\Delta\nu_{\mathrm{iso}}|. \tag{22}$$

Here ν_r is the spinning frequency, $d/2\pi$ is the instantaneous dipole-dipole coupling frequency, $\Delta\nu$ is the difference in the instantaneous chemical shift frequencies, J is the scalar

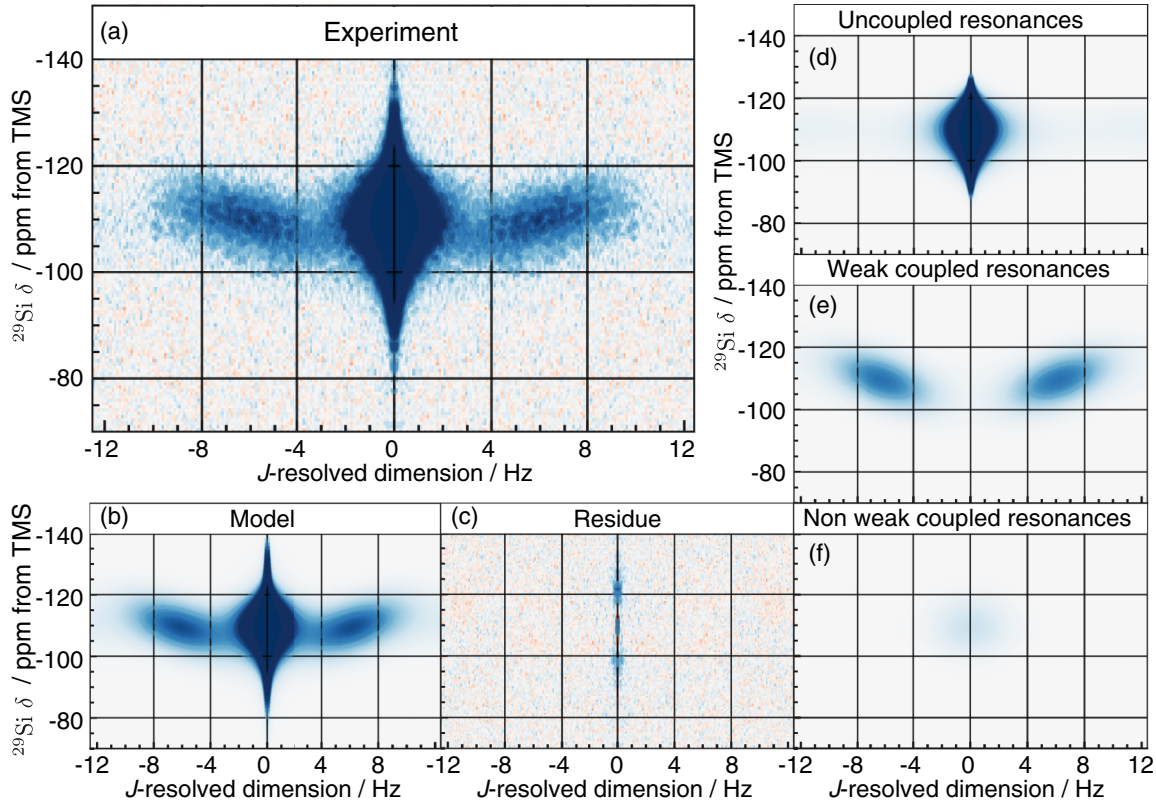

FIG. 2. (a) Natural abundance ^{29}Si-O-^{29}Si 2D J-resolved spectrum of CoO-doped silica glass showing contributions from both coupled and uncoupled ^{29}Si resonances. (b) Simulation and (c) residue obtained from the least-squares minimization of experimental data using model $s(\delta, t_1)$ in Eq (25). (d)–(f) Decomposition of the Fourier transform of the model $s(\delta, t_1)$ in Eq. (25) into (d) uncoupled ^{29}Si spin resonances, (e) weakly coupled ^{29}Si-O-^{29}Si spin resonances, and (f) nonweakly coupled ^{29}Si-O-^{29}Si spin resonances.

coupling frequency, and $\Delta\nu_{\rm iso}$ is the difference in the isotropic chemical shift frequencies of the connected nuclei. On the other hand, under moderate MAS speeds [50],

$$|\Delta\nu_{\rm iso}| \lesssim |\Delta\nu_{\rm ansio}| < |\nu_r| < |d\Delta\nu/2\pi J|, \tag{23}$$

the coupled spins mostly remain within a weak-coupling limit because the CSA ensures that the instantaneous chemical shifts of the coupled spins are different for most of the time even when the two spins have identical isotropic chemical shifts. In Eq. (23), $\Delta\nu_{\rm ansio}$ is the differences in the anisotropic part of the instantaneous chemical shift frequencies.

Because of the disordered network in silica glass, there is a distribution of isotropic chemical shifts as well as CSAs, dipole-dipole, and J couplings. In silica glass, the Q^4 chemical shift anisotropy [51] is on the order of 2 kHz, the dipole-dipole coupling frequency between two ^{29}Si at 3 Å is on the order of 170 Hz, the isotropic chemical shift spans a range of over 2 kHz, and the J coupling varies from 5 to 25 Hz. With $\nu_r = 14.286$ kHz, most of the coupled-spin systems in silica glass would reside within the moderate-MAS condition, Eq. (23), and would result in echoes that are modulated by J coupling as $\cos\pi Jt$, i.e., the weak-coupling limit. Given the strength of all interactions in silica glass, some fraction of the coupled spins—more likely for the higher J couplings—may be in the fast-MAS limit, in which case there will be a finite probability of nonweak couplings. To account for these nonweak resonances we split the doublet relative intensity into

$$P_1 \approx P_{a_0} + P_{a_1}, \tag{24}$$

where P_{a_0} is the relative intensity of weakly coupled ^{29}Si-O-^{29}Si spins, and P_{a_1} is the relative intensity of nonweak couplings.

E. Line shape analysis

As a starting point in our 2D line shape analysis we define $p(J, \delta)$ as the bivariate probability distribution for isotropic ^{29}Si chemical shift and $^2J_{\rm Si\text{-}O\text{-}Si}$ coupling in silica glass. The observed signal can be decomposed into a weighted sum of three contributions from (1) uncoupled ^{29}Si sites, (2) weakly coupled ^{29}Si-O-^{29}Si sites, and (3) nonweakly coupled ^{29}Si-O-^{29}Si sites,

$$\begin{aligned} s(\delta, t_1) =& \big(1 - P_{a_0} - P_{a_1}\big)s_1(\delta, t_1) + P_{a_0}s_2(\delta, t_1) \\ &+ P_{a_1}s_3(\delta, t_1), \end{aligned} \tag{25}$$

where the weights are constrained by the natural abundance ^{29}Si statistics of Eq. (21) and (24).

The first contribution, $s_1(\delta, t)$, from uncoupled ^{29}Si resonances, is modeled as the product

$$s_1(\delta, t_1) = p(\delta)s_{\rm decay}(\delta, t_1), \tag{26}$$

where $p(\delta)$ is the one-dimensional probability distribution for isotropic ^{29}Si chemical shift of silica glass, given by

$$p(\delta) = \int_J p(J, \delta) dJ, \tag{27}$$

and $s_{\text{decay}}(\delta, t_1)$ is a stretched exponential decay in the echo time dimension, t_1, associated with each isotropic chemical shift. The isotropic ^{29}Si line shape of silica glass has been well established [9,51–53] as a skewed distribution. Of the various models that have been proposed to describe this line shape [52], the skew-normal distribution [51,54] has been found to be reasonably accurate. In our analysis, however, any small inaccuracy is of concern because, as stated earlier, the coupled ^{29}Si-O-^{29}Si resonances only account for 16.2% of the total observable resonances. Therefore, any residual modulation from inaccuracies in modeling the uncoupled isotropic ^{29}Si line shape will cause a significant distortion in the extracted ^2J doublet line shape. Thus, we introduce additional flexibility into the isotropic ^{29}Si uncoupled line shape model with a combination of skew-normal and normal distribution functions

$$p(\delta) \approx \underbrace{\frac{C_1}{\Delta_1} e^{-Y_1^2}\{1 + \text{erf}(\alpha_1 Y_1)\}}_{\text{skew-normal}} + \underbrace{\frac{C_2}{\Delta_2} e^{-Y_2^2}}_{\text{normal}}, \tag{28}$$

where

$$Y_i = \frac{\delta - \xi_i}{\sqrt{2}\Delta_i}, \tag{29}$$

and C_i, ξ_i, Δ_i, and α_i are the amplitude, location, scale, and shape parameters, respectively, for the ith distribution. This model gives good agreement with the observed isotropic ^{29}Si line shape, as shown in Fig. S9 of the Supplemental Material [39]. The familiar moments of this distribution—mean isotropic chemical shift, μ_{mas}, the standard deviation, σ_{mas}, the skewness, γ_{mas}, and the excess kurtosis, κ_{mas}—are listed in Table I.

It is well established that NMR relaxation behavior in glasses, specifically low-abundance nuclei like ^{29}Si, are often found to be stretched exponentials with a stretch exponent of $\beta \approx 0.5$—the hallmark of a continuous distribution of relaxation times arising from distant and fluctuating paramagnetic centers [55]. Considering paramagnetic relaxation to be the only dominant mechanism in the silica glass used in our measurement, doped with CoO where Co is the paramagnetic center, we expect a similar stretch exponential behavior for the signal decay along the echo time dimension. We further observe a differential stretch exponential relaxation across ^{29}Si isotropic chemical shift sites ranging from −95 ppm to −125 ppm with a slight linear variation in the stretch exponent from 0.6 to 0.5, respectively. This is modeled as

$$s_{\text{decay}}(\delta, t_1) = \exp\left\{-\left(\frac{t_1 + 4\tau}{T_2}\right)^{\beta(\delta)}\right\}, \tag{30}$$

where the stretch exponent is given by

$$\beta(\delta) = c_\beta + m_\beta(\delta - \mu_\delta), \tag{31}$$

with c_β and m_β as the corresponding intercept and slope, respectively, and T_2 is the transverse dephasing time constant. The term 4τ is added in Eq. (30) because t_1 is referenced to zero at the first echo whereas the signal starts relaxing after the first $\pi/2$ pulse, i.e., a period of 4τ before the detection of first echo. Here, μ_δ is the mean ^{29}Si isotropic chemical shift.

The second echo train signal contribution, $s_2(\delta, t_1)$, from the weakly coupled ^{29}Si-O-^{29}Si resonances for a given chemical shift is given by

$$s_2(\delta, t_1) = \left[\int_J p_w(J, \delta)\cos(\pi J t_1) dJ\right] s_{\text{decay}}(\delta, t_1), \tag{32}$$

where $p_w(J, \delta)$ is the bivariate probability distribution of $^2J_{\text{Si-O-Si}}$ couplings and isotropic chemical shifts from the weakly coupled ^{29}Si nuclei in silica glass. For $s_2(\delta, t_1)$ we find it sufficient to approximate $p_w(J, \delta)$ as a bivariate normal distribution with a correlation coefficient $r_{J,\delta}$. One can then express $s_2(\delta, t_1)$ (see Supplemental Material [39]) as

$$s_2(\delta, t_1) = \underbrace{\frac{N}{\sigma_\delta}\exp\left[-\frac{(\delta - \mu_\delta)^2}{2\sigma_\delta^2}\right]}_{\text{coupled } ^{29}\text{Si lineshape}} \underbrace{\exp\left[-\frac{1}{2}\pi^2 t_1^2 \sigma_J^2\left(1 - r_{J,\delta}^2\right)\right]}_{J\text{-distribution}} \times \cos[\pi t_1 J(\delta)] s_{\text{decay}}(\delta, t_1), \tag{33}$$

where $N = [C_1 + C_2]$ and

$$J(\delta) = r_{J,\delta}\frac{\sigma_J}{\sigma_\delta}(\delta - \mu_\delta) + \mu_J. \tag{34}$$

The first part in Eq. (33) refers to the ^{29}Si isotropic chemical shift line shape arising from coupled ^{29}Si-O-^{29}Si resonances and is described by a normal distribution with mean μ_δ and standard deviation σ_δ. The second part describes a normal distribution of J coupling with mean μ_J and standard deviation σ_J. The cosine term describes the time domain oscillation and $s_{\text{decay}}(\delta, t)$ simulates the signal decay as given in Eq. (30).

Similarly, the third contribution, $s_3(\delta, t_1)$, from the non-weakly coupled ^{29}Si-O-^{29}Si resonances, is modeled as the product

$$s_3(\delta, t_1) = \underbrace{\frac{N}{\sigma_\delta}\exp\left[-\frac{(\delta - \mu_\delta)^2}{2\sigma_\delta^2}\right]}_{\text{coupled } ^{29}\text{Si line shape}} \times \exp\left[-\frac{\pi^2\sigma_s^2 t_1^2}{2}\right] s_{\text{decay}}(\delta, t_1), \tag{35}$$

which shares the same ^{29}Si isotropic chemical shift line shape as the weakly coupled resonances, and experiences an additional decay during the echo time which follows a Gaussian dependence with standard deviation σ_s.

The experimental data were subjected to a least-squares minimization with the full model of Eq. (25) using

TABLE I. Moment analysis of uncoupled ^{29}Si isotropic MAS line shape from model $p(\delta)$ in Eq. (28) where μ_n is the nth moment.

Moments	Description	Value
$\mu_{\text{mas}} = \mu_1$	mean	− 109.63 ppm
$\sigma_{\text{mas}} = \sqrt{\mu_2}$	standard deviation	6.45 ppm
$\gamma_{\text{mas}} = \mu_3/\sigma_{\text{mas}}^3$	skewness	0.06
$\kappa_{\text{mas}} = \mu_4/\sigma_{\text{mas}}^4 - 3$	excess kurtosis	1.42

TABLE II. Optimized fit parameters and reduced chi squared, χ^2_r, from least-squares minimization of the residuals using model in Eq. (25). The reported uncertainties are twice the standard deviation.

$p(\delta)$				$s_{\text{decay}}(\delta, t)$		$p(J, \delta)$		$s_3(\delta, t)$	
C_1	$(4.21 \pm 0.01) \times 10^7$	C_2	$(4.5 \pm 0.1) \times 10^6$	T_2	0.9669 ± 0.004 s	P_{a_0}	0.144 ± 0.001	P_{a_1}	0.018
ξ_1	-114.16 ± 0.01 ppm	ξ_2	-109.7 ± 0.2 ppm	c_β	0.546 ± 0.001	σ_J	4.55 ± 0.06 Hz	μ_δ	-109.57 ± 0.05 ppm
Δ_1	7.25 ± 0.01 ppm	Δ_2	11.8 ± 0.2 ppm	m_β	(0.00326 ± 0.00005)/ppm	μ_J	12.51 ± 0.06 Hz	σ_δ	6.2 ± 0.04 ppm
α_1	1.283 ± 0.008					$r_{J,\delta}$	-0.51 ± 0.01	σ_s	3.3 ± 0.2 Hz
									$\chi^2_r = 2.5$

PYTHON's LMFIT [56] module. All data modeling and spectral analysis were performed with code written in PYTHON 3 [57]. The graphics were produced using PYTHON's MATPLOTLIB library [58]. The optimized fit parameters along with reduced chi squared are listed in Table II. Note that the mean and standard deviations in Tables I and II, for the uncoupled and coupled isotropic line shapes, respectively, are approximately identical. The best-fit simulation and residuals after a Fourier transformation along the echo time dimension, t_1, are presented in Fig. 2.

F. Mapping to Si-O-Si bond angle distribution

The dependence of the $^2J_{\text{Si-O-Si}}$ coupling on local structure in two connected Q^4 was recently examined using first-principles DFT calculations [32]. The two main influences on $^2J_{\text{Si-O-Si}}$ were found to be a primary dependence on the linkage Si-O-Si angle and a secondary dependence on a double mean of Si-O-Si linkage angles of the two connecting tetrahedra Q^4_i and Q^4_j containing the coupled ^{29}Si nuclei. Here, the double mean is given by

$$\overline{\langle\Omega\rangle} = \frac{\langle\Omega\rangle_i + \langle\Omega\rangle_j}{2} = \frac{1}{8}\left(2\Omega_0 + \sum_{k=1}^{6}\Omega_k\right), \tag{36}$$

where $\langle\Omega\rangle_i$ and $\langle\Omega\rangle_j$ are mean Si-O-Si bond angles at Q^4_i and Q^4_j, respectively, and given by

$$\langle\Omega\rangle_i = \frac{1}{4}\sum_{k=0,1,2,3}\Omega_k, \text{ and } \langle\Omega\rangle_j = \frac{1}{4}\sum_{k=0,4,5,6}\Omega_k. \tag{37}$$

In this numbering scheme the six outer Si-O-Si linkage angles correspond to $k \neq 0$. Following these definitions the $^2J_{\text{Si-O-Si}}$ can be related to the Q^4_i-Q^4_j intertetrahedral linkage angle, Ω_0, according to

$$\Omega_0(J, \overline{\langle\Omega\rangle}) = a_J + b_J\left(\frac{J - J_0}{m_1\overline{\langle\Omega\rangle}}\right) + c_J \exp\left\{d_J\left(\frac{J - J_0}{m_1\overline{\langle\Omega\rangle}}\right)\right\}. \tag{38}$$

The coefficients a_J, b_J, c_J, d_J, J_0, and m_1 determined previously [32] are given in Table III. Note that this expression requires both $^2J_{\text{Si-O-Si}}$ and the double mean, $\overline{\langle\Omega\rangle}$, of the Q^4_i-Q^4_j pair to determine Ω_0.

There is an established linear relationship [53,59,60] between ^{29}Si isotropic chemical shift δ of a Q^4 site and its mean Si-O-Si angle,

$$\langle\Omega\rangle = (\delta - b_\delta)/a_\delta, \tag{39}$$

with coefficients, a_δ and b_δ, given in Table III. From this one readily obtains

$$\overline{\langle\Omega\rangle} = (\bar{\delta} - b_\delta)/a_\delta, \tag{40}$$

where $\bar{\delta} = \frac{1}{2}(\delta_i + \delta_j)$ is the mean ^{29}Si isotropic chemical shift, and δ_i and δ_j are the ^{29}Si isotropic chemical shifts of Q^4_i and Q^4_j, respectively. Thus, Eqs. (38) and (40) can be combined to map $p(J, \bar{\delta})$ into $p(\Omega_0, \overline{\langle\Omega\rangle})$. While this mapping requires $p(J, \bar{\delta})$, the line shape analysis of the 2D J-resolved spectrum only provides $p_w(J, \delta)$. To proceed it is necessary to make the approximation $p(J, \delta) \approx p_w(J, \delta)$. Based on the values of $P_{a_0} = 0.144$ and $P_{a_1} = 0.018$ from the experimental line shape analysis this would suggest a loss of intensity due to the nonweakly coupled sites as 11.1%. This loss will be strongest at the highest J couplings. Therefore, this approximation is likely to reduce intensity in the Si-O-Si bond angle distribution at the higher angles. Note that this loss can be diminished by performing measurements at higher magnetic field strengths and using longer interecho periods.

We begin the analysis by determining $p(J, \bar{\delta})$ from $p(J, \delta)$ through the coordinate transformations

$$\text{Series A: } p(J, \delta) \overset{A1}{\Longrightarrow} p(J, \delta_i, \delta_j) \overset{A2}{\Longrightarrow} p(J, \bar{\delta}) \ .$$

Step A1. Given that $p(J, \delta)$ is approximately a bivariate normal distribution we assume that we can construct $p(J, \delta_i, \delta_j)$, a trivariate normal distribution of silica glass, imposing the restrictions that

$$p(\delta_i) = \int p(J, \delta_i, \delta_j) dJ d\delta_j = \int p(J, \delta) dJ = p(\delta),$$
$$p(\delta_j) = \int p(J, \delta_i, \delta_j) dJ d\delta_i = \int p(J, \delta) dJ = p(\delta).$$

TABLE III. Coefficients used in Eqs. (40) and (38) for mapping the mean chemical shift and $^2J_{\text{Si-O-Si}}$ coupling into the double-mean Si-O-Si angle of the two Q^4 involved in coupling and the linkage Si-O-Si angle of the two coupled nuclei.

Coefficient	Value	Coefficient	Value
a_J	107.88°	b_J	223.49°
c_J	0.00002487°	d_J	53.01
m_1	0.778 Hz/deg	J_0	− 7.5 Hz
a_δ	−0.6148 ppm/deg	b_δ	− 19.297 ppm

This leads to a covariance matrix for $p(J, \delta_i, \delta_j)$ given by

$$\boldsymbol{V}_{J,\delta_i,\delta_j} = \begin{bmatrix} \sigma_J^2 & r_{J,\delta}\sigma_J\sigma_\delta & r_{J,\delta}\sigma_J\sigma_\delta \\ r_{J,\delta}\sigma_J\sigma_\delta & \sigma_\delta^2 & r_{\delta_i,\delta_j}\sigma_\delta^2 \\ r_{J,\delta}\sigma_J\sigma_\delta & r_{\delta_i,\delta_j}\sigma_\delta^2 & \sigma_\delta^2 \end{bmatrix}, \tag{41}$$

and a mean vector of $\boldsymbol{\mu}_{J,\delta_i,\delta_j} = [\mu_J, \mu_\delta, \mu_\delta]^T$ where the superscript ^{T} represents the transpose. The only unknown parameter in the covariance matrix $\boldsymbol{V}_{J,\delta_i,\delta_j}$ is the correlation coefficient, $-1 \leqslant r_{\delta_i,\delta_j} \leqslant 1$, between the ^{29}Si isotropic chemical shift distributions $p(\delta_i)$ and $p(\delta_j)$.

Since Q_i^4 and Q_j^4 share a common angle, i.e., Ω_0, their mean angle distributions, $p(\langle\Omega\rangle_i)$ and $p(\langle\Omega\rangle_j)$, will be correlated even when the individual bond angle distributions, i.e., $p(\Omega_k)$, are uncorrelated. In the Appendix we derive approximate expected relationships between the variances and covariances of Ω_0, $\langle\Omega\rangle_i$, $\langle\Omega\rangle_j$, and $\overline{\langle\Omega\rangle}$ with an initial assumption of a seven-dimensional normal distribution correlating all seven angles. In this assumption we further take the individual bond angle distributions, $p(\Omega_k)$, as identical, and correlated to each other with correlation coefficient r if the Si-O-Si bond angles share a Si, and with correlation coefficient r' if not. This leads to a covariance matrix for the bivariate distribution, $p(\langle\Omega\rangle_i, \langle\Omega\rangle_j)$, given by

$$\boldsymbol{V}_{\langle\Omega\rangle_i,\langle\Omega\rangle_j} = \frac{\sigma_\Omega^2}{4}\begin{bmatrix} (3r+1) & \frac{1}{4}(6r+9r'+1) \\ \frac{1}{4}(6r+9r'+1) & (3r+1) \end{bmatrix}, \tag{42}$$

where σ_Ω^2 is the variance of the individual bond angle distribution. The corresponding correlation coefficient is given by

$$r_{\langle\Omega\rangle_i,\langle\Omega\rangle_j} = \frac{6r+9r'+1}{4(3r+1)}. \tag{43}$$

From this expression one can show that uncorrelated individual bond angle distributions, i.e., $r = r' = 0$, lead to a correlation coefficient between the two mean angle distributions of $r_{\langle\Omega\rangle_i,\langle\Omega\rangle_j} = 0.25$. The linear relationship between δ and $\langle\Omega\rangle$ leads to

$$r_{\delta_i,\delta_j} = r_{\langle\Omega\rangle_i,\langle\Omega\rangle_j}. \tag{44}$$

Thus, we expect $r_{\delta_i,\delta_j} = 0.25$ when the individual bond angle distributions, i.e., $p(\Omega_k)$, are uncorrelated.

Similarly, the seven-dimensional normal distribution also leads to the covariance matrix for the bivariate distribution, $p(\Omega_0, \overline{\langle\Omega\rangle})$, given by

$$\boldsymbol{V}_{\Omega_0,\overline{\langle\Omega\rangle}} = \sigma_\Omega^2\begin{bmatrix} 1 & \frac{1}{4}(3r+1) \\ \frac{1}{4}(3r+1) & \frac{1}{32}(18r+9r'+5) \end{bmatrix}, \tag{45}$$

with a corresponding correlation coefficient given by

$$r_{\Omega_0,\overline{\langle\Omega\rangle}} = \frac{\sqrt{2}(3r+1)}{\sqrt{18r+9r'+5}}. \tag{46}$$

We will refer back to these last two results in later steps of this analysis.

Step A2. The distribution $p(J, \delta_i, \delta_j)$ is mapped to distribution $p(J, \overline{\delta})$ following the linear coordinate transformation

$$\begin{bmatrix} J \\ \overline{\delta} \end{bmatrix} = \underbrace{\begin{bmatrix} 1 & 0 & 0 \\ 0 & \frac{1}{2} & \frac{1}{2} \end{bmatrix}}_{\boldsymbol{A}_1}\begin{bmatrix} J \\ \delta_i \\ \delta_j \end{bmatrix}, \tag{47}$$

where $\boldsymbol{A}_1$ is the projection matrix that projects the distribution $p(J, \delta_i, \delta_j)$ onto the diagonal $\delta_i = \delta_j$. The mean vector of the $p(J, \overline{\delta})$ distribution becomes

$$\boldsymbol{\mu}_{J,\overline{\delta}} = \boldsymbol{A}_1 \cdot \boldsymbol{\mu}_{J,\delta_i,\delta_j} = [\mu_J, \mu_\delta]^T, \tag{48}$$

and the covariance matrix becomes

$$\boldsymbol{V}_{J,\overline{\delta}} = \boldsymbol{A}_1 \cdot \boldsymbol{V}_{J,\delta_i,\delta_j} \cdot \boldsymbol{A}_1^T = \begin{bmatrix} \sigma_J^2 & r_{J,\delta}\sigma_J\sigma_\delta \\ r_{J,\delta}\sigma_J\sigma_\delta & \sigma_\delta^2\frac{(1+r_{\delta_i,\delta_j})}{2} \end{bmatrix}, \tag{49}$$

with the correlation coefficient

$$r_{J,\overline{\delta}} = \frac{r_{J,\delta}\sqrt{2}}{\sqrt{1+r_{\delta_i,\delta_j}}}. \tag{50}$$

To obtain the Si-O-Si angle distribution, $p(\Omega_0)$, we continue with the following transformations:

$$\text{Series B: } p(J, \overline{\delta}) \overset{B1}{\Longrightarrow} p(J, \overline{\langle\Omega\rangle}) \overset{B2}{\Longrightarrow} p\left(\Omega_0, \overline{\langle\Omega\rangle}\right) \ .$$

Step B1. We transform $p(J, \overline{\delta})$ to $p(J, \overline{\langle\Omega\rangle})$ using Eq. (40). In matrix notation this linear coordinate transformation is represented as

$$\begin{bmatrix} J \\ \overline{\langle\Omega\rangle} \end{bmatrix} = \underbrace{\begin{bmatrix} 1 & 0 \\ 0 & \frac{1}{a_\delta} \end{bmatrix}}_{\boldsymbol{A}_2}\begin{bmatrix} J \\ \overline{\delta} \end{bmatrix} + \underbrace{\begin{bmatrix} 0 \\ -\frac{b_\delta}{a_\delta} \end{bmatrix}}_{\mathbf{b}_2}. \tag{51}$$

Here $\boldsymbol{A}_2$ is the affine transformation matrix and $\mathbf{b}_2$ is a constant vector. The mean vector of the $p(J, \overline{\langle\Omega\rangle})$ distribution follows as

$$\boldsymbol{\mu}_{J,\overline{\langle\Omega\rangle}} = \boldsymbol{A}_2 \cdot \boldsymbol{\mu}_{J,\overline{\delta}} = \left[\mu_J, \frac{\mu_\delta - b_\delta}{a_\delta}\right]^T, \tag{52}$$

and the covariance matrix becomes

$$\boldsymbol{V}_{J,\overline{\langle\Omega\rangle}} = \boldsymbol{A}_2 \cdot \boldsymbol{V}_{J,\overline{\delta}} \cdot \boldsymbol{A}_2^T = \begin{bmatrix} \sigma_J^2 & r_{J,\delta}\sigma_J\frac{\sigma_\delta}{a_\delta} \\ r_{J,\delta}\sigma_J\frac{\sigma_\delta}{a_\delta} & \frac{\sigma_\delta^2}{a_\delta^2}\frac{(1+r_{\delta_i,\delta_j})}{2} \end{bmatrix}. \tag{53}$$

Step B2. The final transformation from the $p(J, \overline{\langle\Omega\rangle})$ to $p(\Omega_0, \overline{\langle\Omega\rangle})$ distribution is performed numerically using the nonlinear transformation in Eq. (38). For this we first construct the two-dimensional probability distribution $p(J, \overline{\langle\Omega\rangle})$

from $\boldsymbol{\mu}_{J,\overline{\langle\Omega\rangle}}$ and $\boldsymbol{V}_{J,\overline{\langle\Omega\rangle}}$ following

$$p(J,\overline{\langle\Omega\rangle}) = \frac{\exp\left\{-\frac{1}{2}(\mathbf{x}-\boldsymbol{\mu}_{J,\overline{\langle\Omega\rangle}})^T\cdot[\boldsymbol{V}_{J,\overline{\langle\Omega\rangle}}]^{-1}\cdot(\mathbf{x}-\boldsymbol{\mu}_{J,\overline{\langle\Omega\rangle}})\right\}}{2\pi\sqrt{\det(\boldsymbol{V}_{J,\overline{\langle\Omega\rangle}})}}, \tag{54}$$

where $\mathbf{x}=[J,\overline{\langle\Omega\rangle}]^T$ and "det" denotes matrix determinant. From the $p(J,\overline{\langle\Omega\rangle})$ distribution, we determine the $p(\Omega_0,\overline{\langle\Omega\rangle})$ distribution following

$$p(\Omega_0,\overline{\langle\Omega\rangle}) = \int_J p(J,\overline{\langle\Omega\rangle})D[\Omega_0-\Omega_0(J,\overline{\langle\Omega\rangle})]dJ, \tag{55}$$

where the function $D[\cdots]$ denotes the Dirac delta function and function $\Omega_0(\cdots)$ is given by Eq. (38).

In principle, this entire mapping only requires the introduction of one additional parameter, r_{δ_i,δ_j}, the correlation coefficient between the isotropic chemical shift distributions, while the other statistical parameters characterizing $p(J,\delta)$ are determined from the experimental spectrum and given in Table II. Performing this analysis of the experimental results with just these assumptions, however, results in the statistics of

$$p(\Omega_0) = \int p(\Omega_0,\overline{\langle\Omega\rangle})d\overline{\langle\Omega\rangle} \tag{56}$$

not being consistent with

$$p(\overline{\langle\Omega\rangle}) = \int p(\Omega_0,\overline{\langle\Omega\rangle})d\Omega_0 \tag{57}$$

for any value of r_{δ_i,δ_j}. To highlight this point we take $r_{\delta_i,\delta_j}=0.25$ which corresponds to $r=r'=0$ and obtain $\mu_\Omega=146.8^\circ$ and $\mu_{\overline{\langle\Omega\rangle}}=146.8^\circ$, and $\sigma_\Omega=10.64^\circ$ and $\sigma_{\overline{\langle\Omega\rangle}}=8.0^\circ$ from the analysis of the experimental spectrum. While the two means are consistent, the two standard deviations are not. This can be seen by calculating the expected double-mean standard deviation using Eq. (45) with $r=r'=0$ where one obtains

$$\sigma_{\overline{\langle\Omega\rangle}} = \sqrt{\frac{5}{32}}\sigma_\Omega. \tag{58}$$

Thus, if the standard deviation of $p(\overline{\langle\Omega\rangle})$ from the experimental 2D spectrum analysis has a standard deviation of $\sigma_{\overline{\langle\Omega\rangle}}=8.0^\circ$ then one would expect the standard deviation of $p(\Omega_0)$ to be $\sigma_\Omega=20.2^\circ$, a value that is significantly larger than the expected value of $\sigma_\Omega=10.64^\circ$. This statistical inconsistency remains no matter what values of r and r' are investigated.

We believe the series of transformations given here are conceptually correct and that the source of the statistical inconsistency is the use of an incomplete relationship for ^{29}Si isotropic chemical shift to local structure around Q^4. Specifically, there is a less established additional dependence on mean Si-O distance, which is commonly overlooked but noticed in porous siliceous zeolites by Lewis *et al.* [61]. They report an improved relationship between ^{29}Si isotropic chemical shift and the local Q^4 structure given by

$$\delta = b'_\delta + \frac{a'_\delta}{4}\sum_k\left(\langle d_{\text{Si-O},k}\rangle\frac{\cos\Omega_k}{\cos\Omega_k-1}\right), \tag{59}$$

where $\langle d_{\text{Si-O},k}\rangle$ is the mean Si-O bond distance of Si-O-Si linkage with angle Ω_k. The summation over index k denotes all four Si-O-Si bond angles of the Q^4. The values $a'_\delta=-216.95$ ppm/Å and $b'_\delta=48.54$ ppm were obtained by Lewis *et al.* [61] after calibrating with respect to high-silica zeolites ZSM-5(RT), ZSM-5(HT), ferrierite(RT), and ferrierite(HT) where RT = room temperature and HT = high temperature, and the dense-phase SiO_2 polymorphs, quartz and cristobalite. The reason why this relationship is often overlooked, and why the previous relationships between chemical shift and mean Si-O-Si angle alone has applied so well in crystalline silicates, is due to the coexistence of a strong correlation between Si-O distance and Si-O-Si angle [62,63]. A similar issue arose in early efforts to determine the relationship between the ^{17}O quadrupolar coupling constant and the Si-O-Si angle in silicates. In those studies the influence of the Si-O distance was included only through its parametric dependence on the Si-O-Si angle which was conventionally thought to vary according to a negative correlation discovered in crystalline silica polymorphs and further supported by potential energy surfaces determined in *ab initio* studies of small silicate clusters [62,63]. Instead of assuming this correlation Clark *et al.* [27] determined a relationship for the ^{17}O quadrupolar coupling constant that explicitly includes both Si-O distance and Si-O-Si angle and calibrated this expression with experimental ^{17}O results from crystalline silica polymorphs, coesite, α-quartz, cristobalite, and ferrierite(RT). Armed with this relationship Clark and others [28,29] discovered a counterintuitive result from the ^{17}O DAS spectrum of silica glass showing a positive correlation between Si-O distance and Si-O-Si angle. Thus, to proceed in our analysis we assume a line of regression in the correlation between $\langle d_{\text{Si-O},k}\rangle$ and Ω_k in silica glass of the form

$$\langle d_{\text{Si-O},k}\rangle = d^\circ_{\text{Si-O}} + m_\Omega(\Omega_k-\Omega^*), \tag{60}$$

where $\Omega^*=150^\circ$. As shown in the Appendix, one can invoke Eq. (60) and linearize Eq. (59) about $\Omega^*=150^\circ$ as

$$\delta = \underbrace{\left[\Lambda_0 d^\circ_{\text{Si-O}}+\Lambda_1 m_\Omega\right]}_{a_\delta}\langle\Omega\rangle + \underbrace{\left[b'_\delta+\Lambda_2 d^\circ_{\text{Si-O}}+m_\Omega\Lambda_3\right]}_{b_\delta}. \tag{61}$$

Equation (61) shows how the slope and intercept of the linear relationship between ^{29}Si isotropic chemical shift and mean angle $\langle\Omega\rangle$ depend on the trend between the Si-O-Si bond angle Ω and mean Si-O distance $\langle d_{\text{Si-O}}\rangle$, where $\Lambda_0=-0.543716$ ppm/(deg Å), $\Lambda_1=-100.687$ ppm/Å, $\Lambda_2=-19.1295$ ppm/Å, and $\Lambda_3=15\,103.03$ (ppm deg)/Å. In other words, we assume that the ^{29}Si isotropic chemical shift relationship to mean angle has the same function form of Eq. (39) but now with unknown a_δ and b_δ values which depend on the linear trend in the correlation between $\langle d_{\text{Si-O},k}\rangle$ and Ω_k.

Alternatively, one might also call into question the validity of Eq. (38) to account for the statistical inconsistency. Previous investigations of Eq. (38), however, were fairly exhaustive in determining $^2J_{\text{Si-O-Si}}$ behavior in a wide range of cluster geometries—investigating dependencies on Si-O distance, the central Si-O-Si linkage angle, the dihedral angle, and the outer Si-O-Si linkage angles. Thus, we are confident in its accuracy

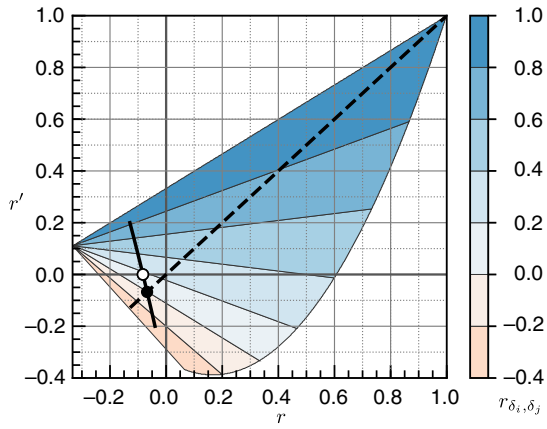

FIG. 3. Shaded area represents the statistically allowed correlation coefficients r and r'. The contour lines with corresponding legend on the right indicate the associated value of the correlation coefficient r_{δ_i,δ_j}. The dotted line corresponds to $r = r'$. The solid line represents the subset of r, r' values where a self-consistent distribution is obtained from the analysis of the experimental 2D spectrum. The closed and open circles represent the two solutions presented in Table IV.

and robustness for interpreting ^2J in both crystalline and glassy materials, regardless of the angle-distance correlation.

Since both $^2J_{\text{Si-O-Si}}$ and $\bar{\delta}$ depend on the same seven Si-O-Si angles associated with the Q_i^4-Q_j^4 linkage we can propose a statistical model that provides the necessary constraints to keep $p(\Omega_0)$ and $p(\overline{\langle\Omega\rangle})$ statistically consistent and, at the same time, calibrate the unknown a_δ and b_δ values of Eq. (61). We begin by writing the covariance matrix derived from the analysis of the experimental spectrum as

$$\boldsymbol{V}^{\{\text{exp}\}}_{\Omega_0,\overline{\langle\Omega\rangle}} = \begin{bmatrix} \sigma^2_{\Omega\text{exp}} & \text{cov}(\Omega_0, \overline{\langle\Omega\rangle})_{\text{exp}} \\ \text{cov}(\Omega_0, \overline{\langle\Omega\rangle})_{\text{exp}} & \frac{\sigma^2_\delta}{a^2_\delta}\frac{(1+r_{\delta_i,\delta_j})}{2} \end{bmatrix}. \quad (62)$$

Because of the linear relationship of Eq. (40) or Eq. (61), the experimental variance of $p(\overline{\langle\Omega\rangle})$ remains the same as in Eq. (53) through the numerical transformation of Eq. (55)—recalling that σ^2_δ is obtained from the experimental isotropic chemical shift line shape. Taking the mean and variance of $p(\Omega_0)$ from experiment as the same as the model,

$$\mu_{\Omega\text{exp}} = \mu_\Omega \quad \text{and} \quad \sigma^2_{\Omega\text{exp}} = \sigma^2_\Omega, \quad (63)$$

we equate the covariance matrices of Eqs. (62) and (45) and obtain the two constraints

$$\text{cov}(\Omega_0, \overline{\langle\Omega\rangle})_{\text{exp}} = \frac{\sigma^2_\Omega}{4}(3r+1), \quad (64)$$

$$\frac{\sigma^2_\delta}{a^2_\delta}\frac{(1+r_{\delta_i,\delta_j})}{2} = \frac{\sigma^2_\Omega}{32}(18r+9r'+5). \quad (65)$$

Substituting the expression of Eq. (43) for r_{δ_i,δ_j} into Eq. (65) leads to the solution

$$r = \frac{4}{3}\left(\frac{\sigma_\delta}{a_\delta\sigma_\Omega}\right)^2 - \frac{1}{3}. \quad (66)$$

Note, there is also an unphysical solution, $r = -(5+9r')/18$, which lies outside the bounds discussed below. For Eqs. (66) and (64) to have a simultaneous solution in r, we substitute Eq. (66) in Eq. (64) and obtain

$$\text{cov}(\Omega_0, \overline{\langle\Omega\rangle})_{\text{exp}} = \frac{\sigma^2_\Omega}{4}(3r+1) = \left(\frac{\sigma_\delta}{a_\delta}\right)^2. \quad (67)$$

In Eq. (67) we have the constraints between the covariance of the experimentally derived distribution, $p(\Omega_0, \overline{\langle\Omega\rangle})$, the model parameters, σ_Ω, r, and the slope a_δ, all of which enforce statistical consistency.

Additionally, we find that the range of the correlation coefficients r and r' can be further constrained with this statistical model. In our analysis we combine the correlation coefficients $r_{\langle\Omega\rangle_i,\langle\Omega\rangle_j}$, r_{δ_i,δ_j}, $r_{J,\delta}$, and $r_{\Omega_0,\overline{\langle\Omega\rangle}}$ in Eqs. (43), (44), (50), and (46), respectively, with the experimentally determined correlation coefficient $r_{J,\delta} = -0.5$ to determine the bounds on $r \in [-\frac{1}{3}, 1]$ and a parametric dependence on r' as

$$r' \in \begin{cases} \left[-1-4r,\ \frac{1}{3}(1+2r)\right], & r \in \left(-\frac{1}{3}, 0\right], \\ \left[\frac{1}{18}(36r^2-12r-6),\ \frac{1}{3}(1+2r)\right], & r \in (0, 1]. \end{cases} \quad (68)$$

This range of allowed values for r and r' is shown as the shaded area in Fig. 3. The associated r_{δ_i,δ_j} is indicated by the shaded contour colors with the corresponding legend on the right.

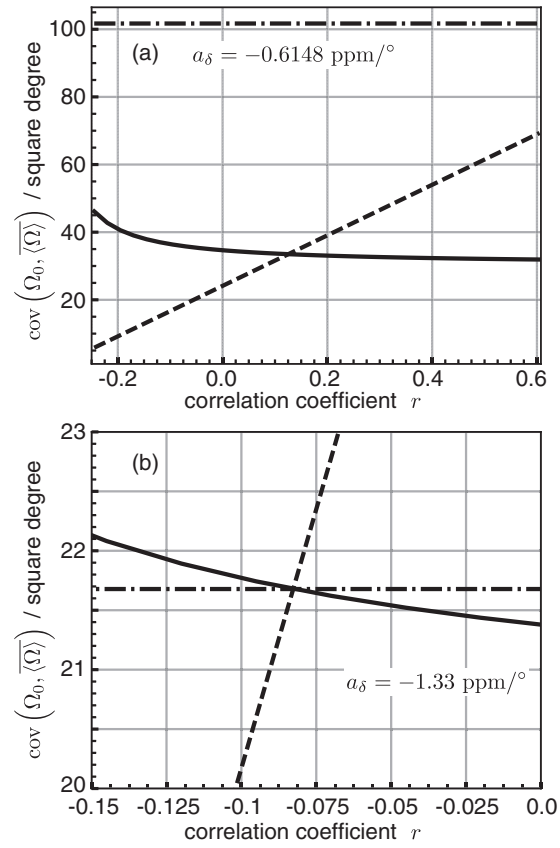

FIG. 4. Comparison of covariance $\text{cov}(\Omega_0, \overline{\langle\Omega\rangle})_{\text{exp}}$ (solid line), parametric dependence on r (dashed line), and $(\sigma_\delta/a_\delta)^2$ (dot-dashed line) when $r' = 0$ where $r \in [-0.25, 0.608]$. In (a) $a_\delta = -0.6148$ ppm/deg and (b) $a_\delta = -1.33$ ppm/deg. In (a), there is no point in r where a self-consistent $p(\Omega_0, \overline{\langle\Omega\rangle})$ distribution is obtained.

Algorithm 1. Iterative algorithm used in this analysis. The convergence is obtained when the absolute tolerance between the three covariances in Eq. (67) is less than 0.005°.

input: a_δ, b_δ, a_J, b_J, c_J, d_J, m_1, J_0 (values from Table III);
assign: r, r';
repeat
  Evaluate r_{δ_i,δ_j}; /* Eq. (43)*/
  Evaluate $\boldsymbol{V}_{J,\overline{\langle\Omega\rangle}}$; /* Eq. (53)*/
  Construct $p(J, \overline{\langle\Omega\rangle})$; /* Eq. (54)*/
  Compute $p(\Omega_0, \overline{\langle\Omega\rangle})$; /* Eq. (55)*/
  Evaluate μ_Ω, σ^2_Ω, $\sigma^2_{\overline{\langle\Omega\rangle}}$, $\mathrm{cov}(\Omega_0, \overline{\langle\Omega\rangle})_{\mathrm{exp}}$;
  Update $r = \frac{4}{3}\left(\frac{\sigma_\delta}{a_\delta\,\sigma_\Omega}\right)^2 - \frac{1}{3}$; /* Eq. (66)*/
  Update $a_\delta = -\frac{\sigma_\delta}{\sqrt{\mathrm{cov}(\Omega_0,\overline{\langle\Omega\rangle})_{\mathrm{exp}}}}$; /* Eq. (67)*/
  Update $b_\delta = \mu_\delta - a_\delta\,\mu_\Omega$;; /*pivot at (μ_δ, μ_Ω)*/
until *convergence*;
end

To illustrate the statistical inconsistency when using the previous relationships between chemical shift and mean Si-O-Si angle alone, we take the slope, $a_\delta = -0.6148$ ppm/deg, calibrated from crystalline silica polymorphs, and plot the three covariances of Eq. (67) in the case of $r' = 0$ in Fig. 4(a). Since solutions to Eq. (67) can only be true at the intersection of all three lines we clearly see that there can be no statistically consistent solution in this particular case.

To find solutions we adopt the iterative approach outlined in Algorithm 1. For each possible value of r' we apply this algorithm to determine the r value that satisfies Eq. (67). The results of this approach, giving all values of r and r' consistent with the experimental spectrum, are shown as the solid black line in Fig. 3. Not all of these solutions, however, are reasonable since a high value of $|r_{\delta_i,\delta_j}|$ would lead to a greater fraction of ^{29}Si-^{29}Si pairs being in the strong J coupling limit. The more likely solutions are in the range near smaller values of $|r_{\delta_i,\delta_j}|$, and, as we will see, result in distribution statistics that are not significantly different. For example, in the case where $r' = 0$ there is a single solution, shown as the open circle in Fig. 3, with $r = -0.082$, $a_\delta = -1.33$ ppm/deg, and $b_\delta = \mu_\delta - a_\delta\mu_\Omega = 87.34$ ppm. Here b_δ is determined through the constraint of the mean of $p(\Omega_0)$ and $p(\overline{\langle\Omega\rangle})$ distributions being identical. This solution is illustrated as the intersection of the three lines in Fig. 4(b) where Eq. (67) is satisfied. This case corresponds to the physical situation where the Si-O-Si angle distributions which do not share a Si are entirely uncorrelated, i.e., $r' = 0$. The resulting distribution $p(\Omega_0, \overline{\langle\Omega\rangle})$ is presented in Fig. 5(a). The projection onto the Ω_0 dimension in Fig. 5(a) gives $p(\Omega_0)$, the Si-O-Si bond angle distribution in silica glass presented as a bold solid line in Fig. 5(c). The statistics of this distribution are given in Table IV. We also present the statistics in Table IV for the consistent solution with $r = r'$ where there is a single solution, shown as the filled circle in Fig. 3, with $r = r' = -0.068$, $a_\delta = -1.3$ ppm/deg, and $b_\delta = 82.54$ ppm. Comparing the two cases in Table IV illustrates the small degree of variation in the parameters along this solid line of solutions.

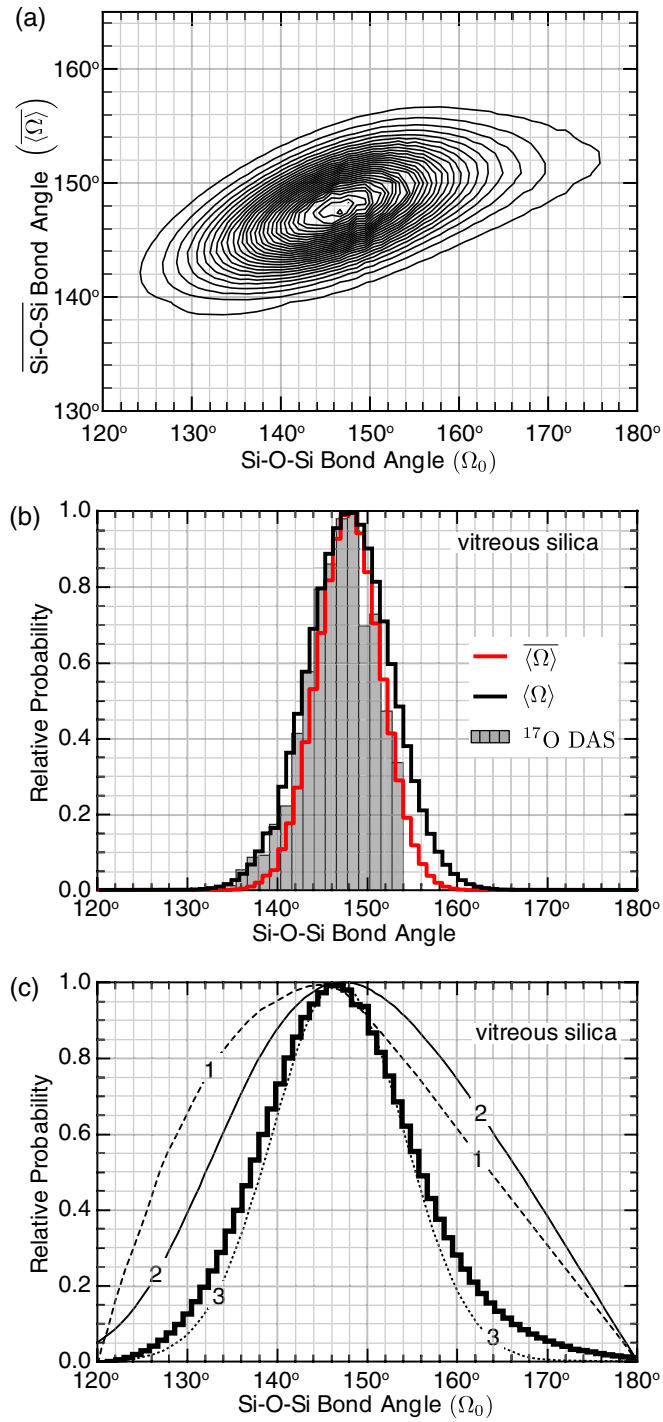

FIG. 5. (a) Correlation between Si-O-Si bond angle Ω_0 and double-average angle $\overline{\langle\Omega\rangle}$ when $r' = 0$. (b) Comparison of double-average Si-O-Si bond angle distributions $\overline{\langle\Omega\rangle}$ against Si-O-Si bond angle distributions from ^{17}O DAS [28]. (c) Comparison of Si-O-Si bond angle distributions from various models. Line 1, XRD Mozzi and Warren model [64]; line 2, HXRD short-range-order (SRO) model [65]; line 3, HXRD/ND Neuefeind and Liss chain [66] model. The bond angle distribution from current work is represented in bold line.

IV. RESULTS AND DISCUSSION

A contour plot of the self-consistent bivariate probability distribution correlating the central Si-O-Si angle of a Q^4-Q^4

TABLE IV. Mean, mode, standard deviations of Si-O-Si bond angle distributions, and correlation coefficients between them for the two models $r' = r$ (left) and $r' = 0$ (right).

Statistic	$r' = r$ response	$r' = 0$ response
$\mu_\Omega = \mu_{\langle\Omega\rangle} = \mu_{\overline{\langle\Omega\rangle}}$	147.8°	147.8°
σ_Ω	10.7°	10.7°
$\sigma_{\langle\Omega\rangle}$	4.8°	4.7°
$\sigma_{\overline{\langle\Omega\rangle}}$	3.4°	3.5°
r	−0.068	−0.082
$r_{\delta_i,\delta_j} = r_{\langle\Omega\rangle_i,\langle\Omega\rangle_j}$	−0.005	0.17
$r_{\Omega,\langle\Omega\rangle}$	0.45	0.43
$r_{\Omega,\overline{\langle\Omega\rangle}}$	0.63	0.57
mode	≈147°	≈147°
a_δ	−1.3 ppm/deg	−1.33 ppm/deg
b_δ	82.54 ppm	87.34 ppm

linkage to its double-mean Si-O-Si angle (seven angles) is given in Fig. 5(a). In Figs. 5(b) and 5(c) are the 1D projections onto dimensions associated with the double-mean Si-O-Si angle and central linkage angle, respectively. The statistics of the bivariate distribution are given in Table IV. Although there is a strong correlation of $r_{\Omega,\overline{\langle\Omega\rangle}} = 0.57$ between these two distributions, this is expected as the central linkage angle is used in defining the double mean of Eq. (36). More noteworthy, however, is the relatively low value of the correlation coefficient, $r = -0.082$, for the four Si-O-Si angles of each Q^4 unit, determined with the underlying model of a septavariate probability distribution of Si-O-Si angles in the Q^4-Q^4 linkage [see Eq. (A1)]. The Si-O-Si angles in silica glass have been commonly assumed as uncorrelated in both diffraction [64–66] and NMR [9,10,53,67,68] analyses, although Malfait *et al.* [69] had argued against this assumption due to ring topology constraints. Here we find experimental confirmation of uncorrelated tetrahedral linkage angles in silica glass.

The 1D Si-O-Si bond angle distribution in silica glass derived from this bivariable distribution [Fig. 5(c)] has a mean at 147.8°, a mode at 147°, and a standard deviation of 10.7°. As mentioned earlier, some intensity at the larger Si-O-Si angles may be lost due to the nonweak couplings which corresponds to ∼11.1% of the total coupled resonances. A selected comparison of bond angle distribution statistics from silica glass obtained from other methods is shown in Table V. The often cited Si-O-Si bond angle distribution of Mozzi and Warren [64] for silica glass is also shown in Fig. 5(c) as line 1. While the mode of 144° falls close to our ^{29}Si ^2J-derived distribution, the width of Mozzi and Warren distribution is significantly wider—an observation that has generally been attributed to incorrect assumptions of uncorrelated angles and distances in Mozzi and Warren's analysis [1,66]. Using assumptions nearly identical to Mozzi and Warren, Poulsen *et al.* [65] used high-energy x-ray measurements of silica glass to obtain the distribution shown as line 2 in Fig. 5(c). Neuefeind and Liss [66] obtained the distribution shown as line 3 in Fig. 5(c) after reanalyzing high-energy x-ray [70] and neutron [71,72] diffraction data of silica glass. They attribute the narrowness of their distribution to a nonuniform distribution of dihedral angles, Si-O-Si-O, but find no evidence of correlation among Si-O distances, Si-O-Si angles, and the dihedral angles. This distribution gives the closest agreement with our ^{29}Si 2D J-resolved spectrum-derived distribution.

An extensive comparison of experimental and molecular dynamics (MD) predicted 1D Si-O-Si bond angle distributions in silica glass was given by Malfait *et al.* [69] in 2008. Overall, there is little agreement among the 1D Si-O-Si bond angle distributions obtained from various MD approaches, and no particular MD approach seems to give consistent agreement with the experimental values obtained here. Unfortunately, the possibility of a full-blown *ab initio* MD simulation of a liquid cooled from the melt into the glassy state is decades away—maybe longer—from our current capabilities. The challenges to classical MD simulations today not only depend on finding accurate potentials but also on obtaining the computational resources to simulate the glass transition at a realistic cooling rate with a realistic number of atoms. *Ab initio* MD methods [73] have advanced significantly in the last decade and hold great promise, particularly in providing accurate potentials; however, this comes at the cost of even greater demands for computational resources which have yet to be realized.

In 2004, Clark *et al.* [28] measured and analyzed the ^{17}O DAS spectrum of silica to obtain an angle distribution that agrees with the mean and mode obtained from our ^{29}Si 2D J-resolved spectral analysis but is considerably narrower in width. As described earlier [29], however, the narrow width from the ^{17}O DAS analysis is an artifact of an oversimplified

TABLE V. Comparison of the mean, mode, and standard deviation of the Si-O-Si bond angle distribution in silica glass obtained from other experimental methods.

Distribution	Method	Bond angle distribution			
		μ_Ω	Mode	σ_Ω	≈FWHM
Mozzi and Warren [64] (1969)	X-ray	147.9° [53]	144°	12.7°	37°
Neuefeind and Liss [66] (1996)	High-energy x-ray	146.7°	146.8	7.3°	17°
Mauri *et al.* [53] (2000)	^{29}Si MAS NMR	151.4°	148°	11.3°	30°
Clark *et al.* [28] (2004)	^{17}O DAS NMR	146.6°	147°	3.8°	10°
Charpentier *et al.* [11] (2009)	^{17}O DAS NMR reanalyzed	147.1°	147°	11.17°	23°
Charpentier *et al.* [11] (2009)	^{29}Si NMR	148.4°		10.8°	23°
This work	^{29}Si-O-^{29}Si J-coupling NMR	147.8°	147°	10.7°	19°

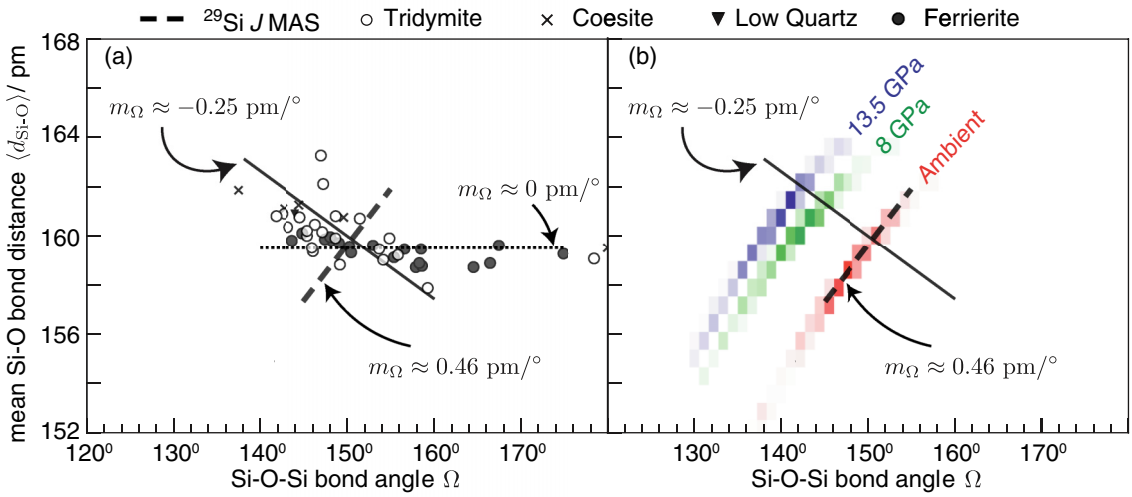

FIG. 6. (a) Correlation of Si-O bond distance and Si-O-Si bond angle for crystalline silica polymorphs along with the positive trend observed in silica glass (dashed black line). The negative angle-distance trend (solid black line) corresponding to $m_\Omega = -0.25$ pm/deg is obtained from low quartz, coesite, and tridymite. The solid black circles correspond to high silica ferrierite structure with the negligible angle-distance trend shown in dotted line, $m_\Omega \approx 0$ pm/deg. (b) Overlay of the 2D histogram correlating mean Si-O bond distance to mean Si-O-Si angle obtained by Trease *et al.* [29] on ambient and densified silica glasses along with the positive trend obtained from the analysis of the 2D J-resolved spectrum.

assumption that each ω_1 (anisotropic) DAS spectrum cross section contains a single site. In reality each ω_1 cross section contains overlapping line shapes arising from a multitude of sites with varying C_q, η_q, and ^{17}O chemical shift. By modeling each cross section with a single site their analysis determines the mean C_q and η_q of each cross section. This biased the overall C_q and η_q distributions obtained from the full 2D spectrum towards a mean C_q and η_q distribution with smaller widths. Therefore, the previous ^{17}O DAS results on silica [28,29] were analyzed in terms of a mean Si-O-Si bond angle distribution, which, as seen in Fig. 5(b), compares favorably to the $\langle\Omega\rangle$ distribution obtained from the J-resolved spectrum. Thus, we expect the correlations and the modes of the distributions obtained with ^{17}O DAS to be accurate. It should be noted that the ^{17}O DAS spectra analysis could be improved to obtain the individual Ω distribution. Such an approach would be highly worthwhile as ^{17}O DAS spectra still provide the most direct measure of the correlation between the distributions of Si-O-Si bond angle and Si-O distance.

In 2009, Charpentier *et al.* [11] reanalyzed the ^{17}O DAS spectrum and employed a more realistic $p(C_q, \eta_q)$ distribution for modeling the ^{17}O DAS and obtained a Si-O-Si distribution that is consistent with our result derived from the ^{29}Si 2D J-resolved spectrum. Charpentier claim no evidence for the positive correlation between Si-O bond distance and Si-O-Si bond angle reported by Clark *et al.* [28], although we would caution that Charpentier's re-calibration of the C_q relationship to Si-O-Si and Si–O distance used only ^{17}O NMR results from quartz, cristobalite, and coesite, and did not include ^{17}O results from any siliceous porous silicates which can have a distinctly different angle-distance correlation.

Finally, we focus on the need to modify the linear relationship between the Q^4 ^{29}Si chemical shift and mean Si-O-Si angle to obtain a self-consistent bivariate distribution from the 2D spectrum correlating ^{29}Si chemical shift and $^2J_{\text{Si-O-Si}}$. As we show in Sec. III F, using the linear relationship of Eq. (39), calibrated on crystalline silica polymorphs, to analyze the experimental ^{29}Si MAS spectrum of silica glass leads to a standard deviation of $\sigma_\Omega = 20.2^\circ$, significantly larger than all values in Table V, including the distribution of Mozzi and Warren. As noted earlier, it is an often overlooked fact that the ^{29}Si isotropic chemical shift of a Q^4 is dependent on both mean Si-O-Si bond angle and mean Si-O distance. Equation (61) further illustrates how the coefficients a_δ and b_δ in Eq. (39) depend on the trend in the correlation between the mean Si-O bond distance and Si-O-Si bond angle given by Eq. (60). A plot of mean Si-O bond distance and Si-O-Si bond angle of various crystalline silica polymorphs is shown in Fig. 6(a) and illustrates the well known negative trend in this particular correlation. This trend approximately follows $m_\Omega = -0.25$ pm/deg, also shown in Fig. 6(a) as the solid black line. It is this value of m_Ω in Eq. (61) that leads to $a_\delta = -0.62$ ppm/deg and $b_\delta = -19.82$ ppm. Interestingly, a similar plot for ferrierite, shown as the solid black symbols in Fig. 6(a), illustrate a different correlation between mean Si-O-Si bond angle and mean Si-O distance, approximately following $m_\Omega \approx 0$ pm/deg, and shown in Fig. 6(a) as the dotted line.

Turning this argument around, we interpret the values of $a_\delta = -1.33$ ppm/deg and $b_\delta = 87.34$ ppm, obtained from our self-consistent analysis of the 2D J-resolved spectrum, using Eq. (61) and find $m_\Omega = 0.459$ pm/deg and $d^\circ_{\text{Si-O}} = 1.596$ Å. This positive trend is shown as the dashed black line in Fig. 6(a) and is nearly orthogonal to the trend from crystalline silica polymorphs. More impressive is the excellent agreement between the trend obtained in this study and that obtained by Trease *et al.* [29] from ^{17}O DAS measurements on an ambient pressure silica glass, shown together in Fig. 6(b). Also shown in Fig. 6(b) are the results of Trease *et al.* [29] on two

other silica glasses densified at 8 and 13.5 GPa. In the three silica glasses of the Trease *et al.* [29] study and the ambient pressure silica glass of the Clark *et al.* [28] study a consistent positive trend in the correlation of Si-O-Si bond angle and Si-O distance is observed in agreement with the results of this study. Our analysis of the ^{29}Si 2D J-resolved spectrum provides an independent confirmation of this positive trend. Unlike the ^{17}O DAS measurements, however, the strength of this positive correlation cannot be determined from the ^{29}Si 2D J-resolved measurement.

Given this growing evidence for a positive correlation between Si-O bond distance and Si-O-Si angle in silica glass, what is its physical origin? Clark *et al.* [28] invoked density fluctuations to explain the positive correlation between Si-O distance and Si-O-Si angle from their ^{17}O DAS results of silica suggesting that smaller angles and distances correspond to higher density regions with smaller rings and vice versa. In this study, however, we find little to no correlation between Si-O-Si angles, i.e., $r \approx 0$, that is, a result that would be inconsistent with this hypothesis of density fluctuations. This positive correlation appears to be something more fundamental to the structure of silica glass and perhaps other fully connected tetrahedral networks. A more plausible explanation, recently proposed by Sen [30], uses the concept of differential entropy to show that a positive correlation between angle and distance has a higher entropy than the negative correlation. And while a positive correlation between distributions is lower in entropy than fully uncorrelated distributions, Sen shows that the combination of entropic and energetic contributions stabilizes the positive correlation in silica glass structure over both uncorrelated or negatively correlated distributions. Overall, this suggests that the notion that SiO_4 tetrahedra in silica glass are structurally identical to those in crystalline silica polymorphs is incorrect.

V. SUMMARY

We have used the shifted-echo PIETA pulse sequence to measure the natural abundance ^{29}Si 2D J-resolved spectrum of silica glass. A full analysis of the NMR transition pathways in this experiment is given as well as a review of the effects of intermediate to strong couplings and the interecho delay times on the J modulated signal measured during echo train acquisition. By working with a ^{29}Si natural abundance sample we find that the doublets from isolated ^{29}Si-^{29}Si pairs are dominant, making the 2D J-resolved spectrum of silica glass more easily analyzed than a ^{29}Si-enriched sample where multiplets are present. It is only through the sensitivity gain of PIETA that such a natural abundance strategy is possible.

Our analysis of the 2D J-resolved spectrum exploits a recently improved understanding [32] of the relationships between geminal J couplings and local structure of a Q^4-Q^4 linkage in which knowledge of both $^2J_{\text{Si-O-Si}}$ coupling and mean ^{29}Si chemical shift of a Q^4-Q^4 linkage can be used to determine its central Si-O-Si linkage angle and the mean (seven) Si-O-Si linkage angle. Even then, this mapping of the 2D J-resolved spectrum of silica glass into the bivariate distribution is not trivial, and requires additional assumptions that (1) the majority of the J couplings are in the weak limit, (2) there is a bivariate normal distribution of ^{29}Si chemical shifts of the two linked Q^4, with a correlation coefficient determined in the mapping, and (3) the statistics of correlated angle distributions can be constrained with the assumption of a multivariate (seven-dimensional) normal distribution of angles in the Q^4-Q^4 linkage. These three assumptions, however reasonable, do not lead to a statistically consistent bivariate probability distribution. Additional flexibility in the mapping must be introduced. This is done by assuming that a line of regression in the correlation between $\langle d_{\text{Si-O}} \rangle$ and Ω in silica glass, using an adjustable slope and intercept, can be combined with a known relationship [61] between isotropic ^{29}Si chemical shift of a Q^4 and its mean Si-O distance and mean Si-O-Si angle. This approach is suggested by the failure of previous attempts to determine the correct Si-O-Si angle distribution width from the ^{29}Si MAS line shape. In other words, any relationship between ^{29}Si chemical shift and mean Si-O-Si angle alone, when calibrated with ^{29}Si chemical shifts of crystalline silicates, will be inappropriate for analyzing the ^{29}Si MAS spectra of silica glass. Only with this added flexibility in the analysis can a statistically consistent bivariate probability distribution correlating the central Si-O-Si angle to the mean Si-O-Si angle be obtained.

From our measurement and analysis of silica glass we determine that the Si-O-Si linkage angles are relatively uncorrelated and that the Si-O-Si angle distribution has a mean at 147.8°, a mode at 147°, and a standard deviation of 10.7°. An unexpected outcome from our analysis is that the line of regression in the correlation between $\langle d_{\text{Si-O}} \rangle$ and Ω in silica needed to obtain this consistent bivariate probability distribution reveals a positive correlation. This confirms a trend previously determined by ^{17}O DAS measurements of ambient pressure and densified silica glasses, and recently interpreted as playing an important entropic role in determining the structure of a fully connected tetrahedral network of silica glass [30].

ACKNOWLEDGMENTS

This material is based upon work supported in part by the National Science Foundation under Grant No. CHE-1506870.

APPENDIX

1. Statistical model

Consider a seven-dimensional multivariate normal Si-O-Si bond angle distribution in silica glass about a Q^4-Q^4 linkage where individual bond angle distributions $p(\Omega_k)$ are assumed to be identically described by a normal distribution with mean μ_Ω and standard deviation σ_Ω. We represent the coordinate of this seven-dimensional space by the vector $\boldsymbol{\Omega} = [\Omega_3, \Omega_2, \Omega_1, \Omega_0, \Omega_4, \Omega_5, \Omega_6]$. Furthermore, an individual bond angle distribution from this seven-dimensional space is assumed to be identically correlated to another bond angle distribution with correlation coefficient r if the Si-O-Si bond angles share a Si. The other bond angle pairs are assumed to be correlated with a correlation coefficient r'. Under these assumptions we write

the covariance matrix of $p(\mathbf{\Omega})$ as

$$\boldsymbol{V}_7 = \sigma_\Omega^2 \begin{bmatrix} 1 & r & r & r & r' & r' & r' \\ r & 1 & r & r & r' & r' & r' \\ r & r & 1 & r & r' & r' & r' \\ r & r & r & 1 & r & r & r \\ r' & r' & r' & r & 1 & r & r \\ r' & r' & r' & r & r & 1 & r \\ r' & r' & r' & r & r & r & 1 \end{bmatrix}. \quad \text{(A1)}$$

Exploiting the properties of linear transformations, we derive analytical expressions for the statistic of $p(\Omega_0, \overline{\langle\Omega\rangle})$ distribution using the covariance matrix $\boldsymbol{V}_7$. We also derive expressions for the statistics of the $p(\langle\Omega\rangle_i, \langle\Omega\rangle_j)$ and $p(\delta_i, \delta_i)$ distributions.

a. $p(\mathbf{\Omega_0}, \overline{\langle\mathbf{\Omega}\rangle})$ *statistics*

Following the definition of Eq. (36) the seven-dimensional Si-O-Si bond angle distribution $p(\mathbf{\Omega})$ is subjected to the following linear coordinate transformation,

$$\begin{bmatrix} \Omega_0 \\ \overline{\langle\Omega\rangle} \end{bmatrix} = \underbrace{\frac{1}{8}\begin{bmatrix} 0 & 0 & 0 & 8 & 0 & 0 & 0 \\ 1 & 1 & 1 & 2 & 1 & 1 & 1 \end{bmatrix}}_{\boldsymbol{M}_1} \mathbf{\Omega}^T, \quad \text{(A2)}$$

where $\boldsymbol{M}_1$ is the coordinate transformation matrix. From $\boldsymbol{M}_1$, we derive the expression for the covariance matrix of $p(\Omega_0, \overline{\langle\Omega\rangle})$ distribution, $\boldsymbol{V}_{\Omega_0, \overline{\langle\Omega\rangle}} = \boldsymbol{M}_1 \cdot \boldsymbol{V}_7 \cdot {\boldsymbol{M}_1}^T$, to obtain the expressions in Eqs. (45) and (46).

b. $p(\langle\mathbf{\Omega}\rangle_i, \langle\mathbf{\Omega}\rangle_j)$ *statistics*

From the definition of Eq. (37) we construct a $p(\langle\Omega\rangle_i, \langle\Omega\rangle_j)$ distribution by performing the following linear coordinate transformation,

$$\begin{bmatrix} \langle\Omega\rangle_i \\ \langle\Omega\rangle_j \end{bmatrix} = \underbrace{\frac{1}{4}\begin{bmatrix} 1 & 1 & 1 & 1 & 0 & 0 & 0 \\ 0 & 0 & 0 & 1 & 1 & 1 & 1 \end{bmatrix}}_{\boldsymbol{M}_2} \mathbf{\Omega}^T, \quad \text{(A3)}$$

where $\boldsymbol{M}_2$ is the transformation matrix. From the covariance matrix for this distribution, $\boldsymbol{V}_{\langle\Omega\rangle\langle\Omega\rangle} = \boldsymbol{M}_2 \cdot \boldsymbol{V}_7 \cdot {\boldsymbol{M}_2}^T$, we obtain Eqs. (42) and (45).

c. $p(\delta_i, \delta_j)$ *statistics*

Using the linear transformation

$$\delta_\lambda = a_\delta \langle\Omega\rangle_\lambda + b_\delta,$$

where $\lambda = i$ or j, the distribution $p(\langle\Omega\rangle_i, \langle\Omega\rangle_j)$ can be mapped to distribution $p(\delta_i, \delta_j)$ when subjected to the following coordinate transformation,

$$\begin{bmatrix} \delta_i \\ \delta_j \end{bmatrix} = \underbrace{\begin{bmatrix} a_\delta & 0 \\ 0 & a_\delta \end{bmatrix}}_{\boldsymbol{M}_3} \begin{bmatrix} \langle\Omega\rangle_i \\ \langle\Omega\rangle_j \end{bmatrix} + \underbrace{\begin{bmatrix} b_\delta \\ b_\delta \end{bmatrix}}_{\mathbf{b}_3}, \quad \text{(A4)}$$

where $\boldsymbol{M}_3$ is the affine transformation matrix and $\mathbf{b}_3$ is a constant vector. The covariance matrix for the $p(\delta_i, \delta_j)$ distribution, $\boldsymbol{V}_{\delta_i,\delta_j} = \boldsymbol{M}_3 \cdot \boldsymbol{V}_{\langle\Omega\rangle_i,\langle\Omega\rangle_j} \cdot {\boldsymbol{M}_3}^T$, is given by

$$\boldsymbol{V}_{\delta_i,\delta_j} = a_\delta^2 \, \boldsymbol{V}_{\langle\Omega\rangle_i,\langle\Omega\rangle_j}, \quad \text{(A5)}$$

and the correlation coefficient of Eq. (44) follows from $\boldsymbol{V}_{\delta_i,\delta_j}$.

2. ^{29}Si chemical shift dependence on Si-O distance

To compare Eq. (59) with the linear relationship in Eq. (39), we consider a linear trend of Eq. (60). Substituting Eq. (60) in Eq. (59), followed by a linearization using a series expansion in Ω_k about Ω^*, we have

$$\begin{aligned} \delta = {} & \left(a'_\delta x_2 d^0_{\text{Si-O}} + a'_\delta x_1 m_\Omega\right)\langle\Omega\rangle + (x_1 a'_\delta - x_2 a'_\delta \Omega^*) d^0_{\text{Si-O}} \\ & - a'_\delta x_1 m_\Omega \Omega^* + b'_\delta, \end{aligned} \quad \text{(A6)}$$

where $x_1 = (2\sqrt{3} - 3)$ and $x_2 = \frac{\pi}{90^\circ}(7 - 4\sqrt{3})$ are coefficients from the series expansion. Here $\langle\Omega\rangle = \frac{1}{4}\sum_k \Omega_k$ is the average Si-O-Si bond angle about the Si tetrahedron. Expanding about $\Omega^* = 150^\circ$ leads to

$$\begin{aligned} \Lambda_0 &= a'_\delta x_2 = -0.543716 \text{ ppm/(deg Å)}, \\ \Lambda_1 &= a'_\delta x_1 = -100.687 \text{ ppm/Å}, \\ \Lambda_2 &= \Lambda_1 - \Lambda_0 \Omega^* = -19.1295 \text{ ppm/Å}, \\ \Lambda_3 &= -\Lambda_1 \Omega^* = 15\,103.03 \text{ (ppm deg)/Å}, \end{aligned} \quad \text{(A7)}$$

and the expression in Eq. (A6) reduces to Eq. (61). Equation (61) shows how the slope and intercept of the linear relationship of Eq. (39) between ^{29}Si isotropic chemical shift and mean angle $\langle\Omega\rangle$ depends on the trend between the Si-O-Si bond angle, Ω, and the mean Si-O distance, $\langle d_{\text{Si-O}}\rangle$.

[1] A. Wright, J. Non-Cryst. Solids **179**, 84 (1994).

[2] A. C. Hannon, Neutron diffraction techniques for structural studies of glasses, in *Modern Glass Characterization* (Wiley-Blackwell, 2015), Chap. 5, pp. 1–83.

[3] P. Biswas, D. N. Tafen, F. Inam, B. Cai, and D. A. Drabold, J. Phys.: Condens. Matter **21**, 084207 (2009).

[4] R. L. McGreevy and L. Pusztai, Mol. Simul. **1**, 359 (1988).

[5] R. L. McGreevy, J. Phys.: Condens. Matter **13**, R877 (2001).

[6] A. Pandey, P. Biswas, and D. A. Drabold, Sci. Rep. **6**, 33731 (2016).

[7] D. A. Drabold, Eur. Phys. J. B **68**, 1 (2009).

[8] M. Eden, Annu. Rep. Prog. Chem., Sect. C: Phys. Chem. **108**, 177 (2012).

[9] E. Dupree and R. F. Pettifer, Nature (London) **308**, 523 (1984).

[10] L. F. Gladden, T. A. Carpenter, and S. R. Elliott, Philos. Mag. B **53**, L81 (1986).

[11] T. Charpentier, P. Kroll, and F. Mauri, J. Phys. Chem. C **113**, 7917 (2009).

[12] I. Farnan, P. J. Grandinetti, J. H. Baltisberger, J. F. Stebbins, U. Werner, M. A. Eastman, and A. Pines, Nature (London) **358**, 31 (1992).

[13] B. F. Chmelka, K. T. Mueller, A. Pines, J. F. Stebbins, Y. Wu, and J. W. Zwanziger, Nature (London) **339**, 42 (1989).

[14] K. T. Mueller, B. Q. Sun, G. C. Chingas, J. W. Zwanziger, T. Terao, and A. Pines, J. Magn. Reson. **86**, 470 (1990).

[15] K. T. Mueller, Y. Wu, B. F. Chmelka, J. Stebbins, and A. Pines, J. Am. Chem. Soc. **113**, 32 (1991).

[16] P. J. Grandinetti, J. H. Baltisberger, A. Llor, Y. K. Lee, U. Werner, M. A. Eastman, and A. Pines, J. Magn. Reson., Ser. A **103**, 72 (1993).

[17] H. K. C. Timken, S. E. Schramm, R. J. Kirkpatrick, and E. Oldfield, J. Phys. Chem. **91**, 1054 (1987).

[18] J. A. Tossell and P. Lazzeretti, Chem. Phys. Lett. **112**, 205 (1987).

[19] J. A. Tossell and P. Lazzeretti, Phys. Chem. Miner. **15**, 564 (1988).

[20] C. G. Lindsay and J. A. Tossell, Phys. Chem. Miner. **18**, 191 (1991).

[21] P. J. Grandinetti, J. H. Baltisberger, U. Werner, A. Pines, I. Farnan, and J. F. Stebbins, J. Phys. Chem. **99**, 12341 (1995).

[22] K. E. Vermillion, P. Florian, and P. J. Grandinetti, J. Chem. Phys. **108**, 7274 (1998).

[23] T. M. Clark and P. J. Grandinetti, Solid State NMR **16**, 55 (2000).

[24] T. M. Clark and P. J. Grandinetti, J. Non-Cryst. Solids **265**, 75 (2000).

[25] T. M. Clark, P. J. Grandinetti, P. Florian, and J. F. Stebbins, J. Phys. Chem. B **105**, 12257 (2001).

[26] T. M. Clark and P. J. Grandinetti, Solid State NMR **27**, 233 (2005).

[27] T. M. Clark and P. J. Grandinetti, J. Phys.: Condens. Matter **15**, S2387 (2003).

[28] T. M. Clark, P. J. Grandinetti, P. Florian, and J. F. Stebbins, Phys. Rev. B **70**, 064202 (2004).

[29] N. M. Trease, T. M. Clark, P. J. Grandinetti, J. F. Stebbins, and S. Sen, J. Chem. Phys. **146**, 184505 (2017).

[30] S. Sen, J. Non-Cryst. Solids **486**, 9 (2018).

[31] J. H. Baltisberger, B. J. Walder, E. G. Keeler, D. C. Kaseman, K. J. Sanders, and P. J. Grandinetti, J. Chem. Phys. **136**, 211104 (2012).

[32] D. J. Srivastava, P. Florian, J. H. Baltisberger, and P. J. Grandinetti, Phys. Chem. Chem. Phys. **20**, 562 (2018).

[33] P. Florian, F. Fayon, and D. Massiot, J. Phys. Chem. C **113**, 2562 (2009).

[34] M. M. Maricq and J. S. Waugh, J. Chem. Phys. **70**, 3300 (1979).

[35] A. Allerhand, J. Chem. Phys. **44**, 1 (1966).

[36] R. Freeman and H. D. W. Hill, J. Chem. Phys. **54**, 301 (1971).

[37] P. J. Grandinetti, J. T. Ash, and N. M. Trease, Prog. Nucl. Magn. Reson. Spectrosc. **59**, 121 (2011).

[38] G. Bodenhausen, H. Kogler, and R. R. Ernst, J. Magn. Reson. **58**, 370 (1984).

[39] See Supplemental Material at http://link.aps.org/supplemental/10.1103/PhysRevB.98.134202 for additional theoretical details on the line shape model for the weak $^2J_{\text{Si-O-Si}}$ couplings, the NMR pulse sequence, signal processing scripts, and the experimental NMR signal data.

[40] J. A. Aguilar, M. Nilsson, G. Bodenhausen, and G. A. Morris, Chem. Commun. **48**, 811 (2012).

[41] K. Takegoshi, K. Ogura, and K. Hikichi, J. Magn. Reson. **84**, 611 (1989).

[42] P. C. van Zijl, C. T. Moonen, and M. von Kienlin, J. Magn. Reson. **89**, 28 (1990).

[43] B. J. Walder, K. K. Dey, M. C. Davis, J. H. Baltisberger, and P. J. Grandinetti, J. Chem. Phys. **142**, 014201 (2015).

[44] Details on how a $\pi/2$ pulse splits each of the eight transition pathways above into 13 pathways, which are then reduced down to only 32 detectable transition pathways at $t = 0$ through constructive and destructive interference of the labeled pairs of transition pathways in Eqs. (10) and (11) above, are given in the Supplemental Material [39].

[45] R. H. Lamoreaux, D. L. Hildenbrand, and L. Brewer, J. Phys. Chem. Ref. Data **16**, 419 (1987).

[46] Z. H. Gan, J. Am. Chem. Soc. **122**, 3242 (2000).

[47] H. T. Kwak and Z. H. Gan, J. Magn. Reson. **164**, 369 (2003).

[48] PhySy, Ltd., RMN 1.1, http://www.physyapps.com.

[49] E. L. Hahn and D. E. Maxwell, Phys. Rev. **88**, 1070 (1952).

[50] L. Duma, W. C. Lai, M. Carravetta, L. Emsley, S. P. Brown, and M. H. Levitt, Chem. Phys. Chem. **5**, 815 (2004).

[51] J. H. Baltisberger, P. Florian, E. G. Keeler, P. A. Phyo, K. J. Sanders, and P. J. Grandinetti, J. Magn. Reson. **268**, 95 (2016).

[52] J. Mahler and A. Sebald, Solid-State NMR **5**, 63 (1995).

[53] F. Mauri, A. Pasquarello, B. G. Pfrommer, Y.-G. Yoon, and S. G. Louie, Phys. Rev. B **62**, R4786 (2000).

[54] A. Azzalini and A. Capitanio, *The Skew-Normal and Related Families*, Institute of Mathematical Statistics Monographs (Cambridge University Press, Cambridge, 2014).

[55] J. R. Bodart, V. P. Bork, T. Cull, H. Ma, P. A. Fedders, D. J. Leopold, and R. E. Norberg, Phys. Rev. B **54**, 15291 (1996).

[56] M. Newville, T. Stensitzki, D. B. Allen, and A. Ingargiola, 10.5281/zenodo.11813.

[57] S. van der Walt, S. C. Colbert, and G. Varoquaux, Comput. Sci. Eng. **13**, 22 (2011).

[58] J. D. Hunter, Comput. Sci. Eng. **9**, 90 (2007).

[59] J. V. Smith and C. S. Blackwell, Nature (London) **303**, 223 (1983).

[60] G. Engelhardt and R. Radeglia, Chem. Phys. Lett. **108**, 271 (1984).

[61] J. R. Lewis, C. C. Freyhardt, and M. E. Davis, J. Phys. Chem. **100**, 5039 (1996).

[62] G. V. Gibbs, Am. Mineral. **67**, 421 (1982).

[63] G. Gibbs, A. Wallace, D. Cox, R. Downs, N. Ross, and K. Rosso, Am. Mineral. **94**, 1085 (2009).

[64] R. L. Mozzi and B. E. Warren, J. Appl. Cryst. **2**, 164 (1969).

[65] H. Poulsen, J. Neuefeind, H. Neumann, J. Schneider, and M. Zeidler, Nucl. Instrum. Methods Phys. Res., Sect. B **97**, 162 (1995).

[66] J. Neuefeind and K.-D. Liss, Ber. Bunsen-Ges. Phys. Chem. **100**, 1341 (1996).

[67] R. Oestrike, W. Yang, R. J. Kirkpatrick, R. L. Hervig, A. Navrotsky, and B. Montez, Geochim. Cosmochim. Acta **51**, 2199 (1987).

[68] R. F. Pettifer, R. Dupree, I. Farnan, and U. Sternberg, J. Non-Cryst. Solids **106**, 408 (1988).

[69] W. J. Malfait, W. E. Halter, and R. Verel, Chemical Geology **256**, 269 (2008).

[70] H. Poulsen, J. Neuefeind, H.-B. Neumann, J. Schneider, and M. Zeidler, J. Non-Cryst. Solids **188**, 63 (1995).

[71] P. A. V. Johnson, A. Wright, and R. N. Sinclair, J. Non-Cryst. Solids **58**, 109 (1983).

[72] D. I. Grimley, A. Wright, and R. N. Sinclair, J. Non-Cryst. Solids **119**, 49 (1990).

[73] D. Marx and J. Hutter, *Ab Initio Molecular Dynamics: Basic Theory and Advanced Methods* (Cambridge University Press, Cambridge, 2009).